Surface uplift and topographic rejuvenation of a tectonically inactive range: Insights from Anti-Atlas and Siroua Massif (Morocco)

Clementucci R.[1,2*], Ballato P.[1], Siame L.[2], Fox M.[3], Lanari R.[1,4], Sembroni A.[1], Faccenna C.[1,5], Yaaqoub A.[6], Essaifi A.[6]

[1] *Dipartimento di Scienze, Università Roma Tre, Largo San Leonardo Murialdo 1, 00146 Rome, Italy.*

[2] *Aix-Marseille Univ., CNRS, IRD, INRAE, Collège de France, CEREGE, Aix-en Provence, France.*

[3] *Department of Earth Sciences, University College London, Gower Street, London, WC1E 6BT, United Kingdom.*

[4] *Dipertimento di scienze, Università di Firenze, Italia.*

[5] *GFZ-German Research Centre for Geosciences, Potsdam, Germany.*

[6] *Département de Géologie, FSSM, B.P. 2390, Universite´ Cadi Ayyad, Marrakech, Morocco.*

Corresponding author: romano.clementucci@uniroma3.it

Key Points:

- Cenozoic topographic rejuvenation shown by the transient state of the stream network and high-standing erosional surface.
- Contribution of regional surface uplift on the rejuvenation of the Anti-Atlas topography due to deep mantle activity.
- Regional uplift increases from the western (500 m) to the central Anti-Atlas (1100 m) and Siroua Massif (1500 m) since middle-late Miocene.

Abstract

The Atlas-Meseta intracontinental orographic system of Morocco experienced recent, large-scale surface uplift as documented by elevated late Miocene, shallow-water marine deposits exposed in the Middle Atlas Mountains. The Anti-Atlas Mountains do not present any stratigraphic records that document regional vertical movements, however, the presence of a high-standing, erosional surface, and the transient state of river networks, provides insights into the uplift history of the belt and the mechanisms that drove it. Here, we combine geomorphic and stream profiles analyses, celerity of knickpoints and linear inverse landscape modelling with available geological evidence, to decipher the spatial and temporal variations of surface uplift in the Anti-Atlas and the Siroua Massif. Our results highlight the presence of a transient landscape, and document a long wave-length topographic swell (~ 100 x 600 km) with a maximum surface uplift of ~1500 m in the Siroua Massif and ~1100 m in the central Anti-Atlas starting from ~10 Ma, in association with late Miocene magmatism in the Siroua and Saghro Massif and contractional deformation in the High Atlas. Uplift rates for the central Anti-Atlas range between 70 and 180 m/Myr, fall within the same

order of the rates obtained from uplifted marine deposits suggesting a similar deep-seated mechanism of uplift most likely related to astenopsheric upwelling. Overall, our approach allows to quantitatively constrain the transient state of the landscape and the contribution of regional surface uplift on mountain building processes.

1. Introduction

The interplay between exogenic and endogenic processes controls the growth and decay of topography over diverse temporal and spatial scales. Topographic development is generated by different mechanisms, such as crustal shortening and thickening, magmatic addition, flexural rebound, and asthenospheric flow, where each process is associated with a typical wavelength (10^{-1} to 10^3 km) and amplitude (10 to 10^3 m; *e.g.*, England and Molnar, 1990; De Celles et al., 2009; Faccenna and Becker, 2020). Topographic decay results from geomorphic erosion, which is primarily controlled by climate, topographic gradients, and rock strength (*i.e.*, Jansen et al., 2010; Scharf et al., 2013; Clementucci et al., 2022). When topographic decay prevails, extensive low-gradient, low-topographic relief landscapes may form (Baldwin et al., 2003; Tucker and van der Beek, 2013). These geomorphic features can be also found at the summit of mountains areas (Miller et al., 2013; West et al., 2013; Calvet et al., 2015), where they have been interpreted to have formed either in situ at high elevation (*e.g.*, Yang et al., 2015; Fox et al., 2020), or to be part of a less elevated and extensive low-relief landscape that has undergone recent surface uplift (*e.g.*, Calvet et al., 2015; Olivetti et al., 2012; 2016; Whipple et al., 2017). In the case of surface uplift, such an elevated paleo-topography, named relict landscape or paleo-surface, represents a transient geomorphic marker that provides a reference frame for quantifying the spatial distribution of surface uplift (Calvet et al., 2015; Fox, 2019). Thus, relict landscapes represent a unique opportunity to decipher the wavelength and the amplitude of surface uplift, and consequently the mechanisms that created such a topography, especially in areas devoid of stratigraphic constraints.

The Atlas-Meseta intracontinental orographic system of Morocco is composed of different morpho-structural domains that from north to south include: the Moroccan Meseta (Western Meseta and Eastern High Plateaus), the Middle Atlas, the High Atlas, the Siroua Massif, and the Anti-Atlas (Figure 1a). The High and Middle Atlas are the main active orogen (*e.g.*, Sebrier et al., 2006), while the other regions are characterized by a relatively high topography that formed without significant crustal deformation (Teixell et al., 2003; Frizon de Lamotte et al., 2009; Pastor et al., 2015). This configuration offers the opportunity to investigate rates, wavelength, magnitudes and causes of large-scale topographic growth.

In this study, we focus on the Anti-Atlas Mountains, a Variscan orogen characterized by a complex assemblage of intrusive, metamorphic, and sedimentary rocks. Similarly to the Appalachian, which represent the American counterpart, the topography of the Anti-Atlas consists of a wide relict landscape that experienced a relatively recent phase of surface uplift (Choubert, 1952; Malusà et al., 2007; Missenard et al., 2008; Guimera et al., 2011; Clementucci et al., 2022). The causes of this topographic rejuvenation are still poorly understood. Some authors suggested that uplift may be related to Cenozoic shortening (Giumera et al., 2011), whereas others proposed the occurrence of deep dynamic processes (Missenard et al., 2006; Sebrier et al., 2006; Frizon de Lamotte et al., 2009). In this context, the absence of tectonic activity, the steady protracted low denudation rates, and the occurrence of an elevated relict landscape offer the possibility to quantify the regional surface uplift in the Anti-Atlas and the Siroua Massif and to investigate possible causal uplift mechanisms.

To achieve these goals, we combined quantitative analysis of regional and basin-scale topography with stream profiles analysis (knickpoints characterization, longitudinal profiles and $-z$ plot) and recently published basin-wide denudation rates inferred from ^{10}Be concentrations (Clementucci et al., 2022). Furthermore, we performed stream projections from the upper relict channel profiles and reconstructed the paleo-landscape to constrain the amount of relative base level fall following the increase in Cenozoic rock uplift rates. Finally, we constrained the timing of this geomorphic rejuvenation to the middle-late Miocene by applying a knickpoints celerity model. This approach provides a framework for discussing the contribution of large-scale, deep signals and shallower processes in generating the regional topographic relief in areas where large wavelength uplift occurs.

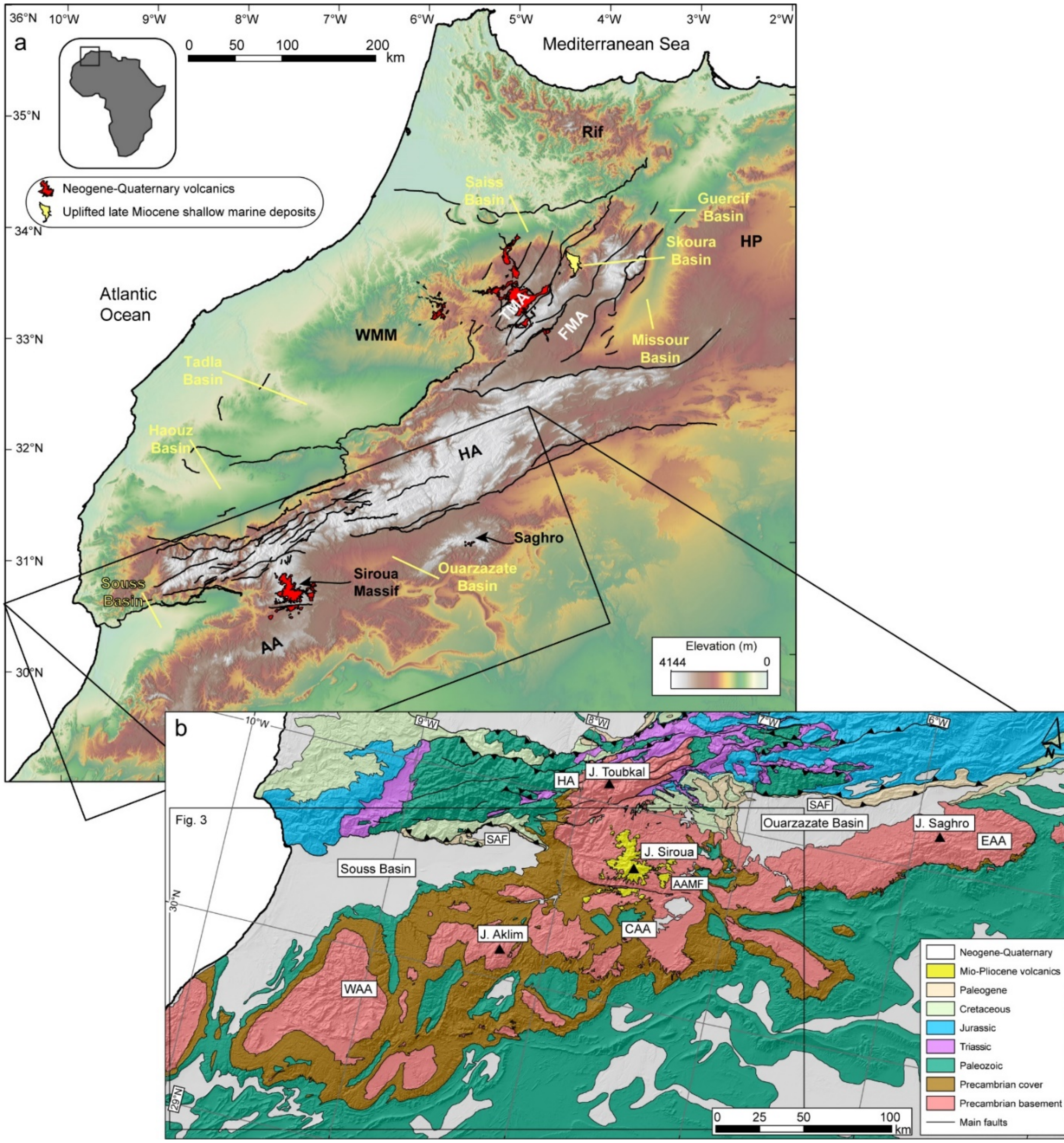

Figure 1. (a) Topographic map of the Atlas-Meseta orographic system and his morpho-structural domains. FMA: Folded Middle Atlas. TMA: Tabular Middle Atlas. HP: High Plateaus. WMM: Western Moroccan Meseta. AA : Anti-Atlas. HA : High Atlas. (b) Simplified geological map of High and Anti-

Atlas Mountains based on the 1:1.000.000 geological map of Morocco (modified from Maroc Service Géologique, 1985). EAA: Eastern Anti-Atlas, CAA: Central Anti-Atlas, WAA: Western Anti-Atlas, AAMF: Anti-Atlas Major Fault, SAF: South Atlas Fault. The main mountain peaks are shown with black triangles.

1. Geological background

(a) Geological setting

The intracontinental Atlas-Meseta orographic system of Morocco is composed of two WSW-ENE oriented mountain belts, the High Atlas (HA) and the Anti-Atlas (AA), and two elevated regions with low-topographic relief, named Western and Eastern (or High Plateaus) Meseta, which are separated by the SW-NE striking Middle Atlas belt (Figure 1a, TMA and FMA). This system of mountain belts experienced a complex geologic history including multiple episodes of contractional deformation and rifting (Froitzheim et al., 1988; Hafid, 2000; Frizon de Lamotte et al. 2000; Domènech et al., 2015). Currently, active deformation is controlled by the plate convergence between Africa and Eurasia (Froitzheim et al., 1988; Hafid, 2000; Frizon de Lamotte et al. 2000; Gomez et al. 2000; Teixell et al., 2003; Lanari et al., 2020b). In the following, we briefly summarize the evolution of the HA, the AA, the Siroua and Saghro Massif, and the adjacents Souss and Ouarzazate basins.

With a few mountain peaks above 4 km of elevation, the HA is the highest domain of the Atlas system that strikes for approximately 600 km over a width of 50 to 100 km. The HA consists of a fold and thrust belt composed of Precambrian, Paleozoic, and Mesozoic rocks (Figure 1). Mesozoic rocks include mostly syn-rift (Jurassic and Triassic) and post-rift deposits (Cretaceous), related to the opening of a rift basin developed during the breakup of Africa (Arboleya et al., 2004; Baudon et al., 2009; Lanari et al., 2020b). Based on thermochronological and structural data the main exhumation episode started in the middle/late Miocene and led to 4-6 km of exhumation (Balestrieri et al., 2009; Barbero et al., 2007; Domènech, 2015; 2016; Ghorbal, 2009; Lanari et al., 2020a; 2020b; Leprêtre et al., 2018; Missenard et al., 2008).

The HA and AA belts are separated by the Souss and the Ouarzazate basins, which have been commonly interpreted as the southern Neogene foreland basins of the HA (Figure 1; Sebrier et al., 2006; Arboleya et al., 2008). The Souss Basin has an eastward wedging geometry and is characterized by a longitudinal, E-W oriented, drainage system flowing directly into the Atlantic Ocean (Figure 2a). The basin extends for a length of more than 150 km and has a rather flat, low-topographic relief morphology that increases progressively toward the basin interior up to ~700 m of elevation. The basin fill includes Pliocene to Quaternary fluvial, fluvio-lacustrine and aeolian sediments derived from the adjacent uplifting HA and AA belts (Hssaine and Bridgland, 2009).

The Ouarzazate Basin lies between 1200 and 1800 m of elevation and extends over a length of more than 150 km (Figure 1). The basin filling consists of a <1-km-thick-succession including Middle Eocene marine deposits unconformably overlain by Mio-Pliocene terrestrial sediments marking the development of endorheic conditions (Fraissinet et al. 1988; Gorler et al. 1988; El Harfi et al., 2001; Teson & Teixell 2006; Teson et al., 2010). The basin is currently drained by the Draa River a southward draining system that crosses the AA through a narrow bedrock gorge and then flows parallel to the AA before entering in the Atlantic Ocean (Figure 2a). The transition from endorheic to exoreic conditions most likely occurred in the Plio-Pleistocene, either through regressive erosion from the southern AA flank (Stablein, 1988) or lake overspill (Arboleya et al., 2008).

The Siroua Massif represents a strato-volcano covering an area of approximately of 500 km^2 and reaching maximum elevation of ~3300 m. Here, the Mio-Pliocene volcanic deposits directly overlie the Precambrian basement, which is characterized by an elongated, dome-like morphology with a low-topographic relief landscape (Missenard et al., 2008; Giumera et al. 2011).

The AA belt extends over approximately 600 km of length, has a width of 100 to 150 km, and rises ~2 km above sea level. The orogen was built through a series of collisional events starting from the Eburnean orogeny at around 2000 Ma (Ait Malek et al., 1998; Thomas et al., 2002; Walsh et al., 2002). Afterward, it experienced two main orogenic events: the Neoproterozoic Pan-African orogeny (Leblanc, 1975; Hefferan et al., 2000; Gasquet et al., 2008) with a subsequent extensional event during the Late Neoproterozoic (Piqué et al., 1999; Soulaimani et al., 2003) and the late Carboniferous Variscan orogeny (Sebti et al., 2009; Soulaimani et al., 2014; Sehrt et al., 2018). Low-temperature thermochronology and stratigraphic data indicate that the AA was not subjected to major Mesozoic vertical movements, while denudation appears to have been rather uniform at rates of ~20 m/Myr since at least the late Cretaceous (Lanari et al., 2020a; Charton et al., 2021; Clementucci et al., 2022). The basement is composed of magmatic, metamorphic, and sedimentary rocks assembled during the Eburnean and Pan-African orogenesis. These rocks are widely exposed along the axial sectors of the range (Figures 1b and S1) and are overlain by a late Precambrian and Paleozoic sedimentary sequence with a thickness of almost 10 km in the Western AA decreasing to less than 6 km in the eastern sectors of the belt (Piqué and Michard, 1989; Helg et al., 2004; Burkhard et al., 2006). This sedimentary cover was predominantly deposited in a shallow-water marine environment during the post Pan-African extensional event (Azizi Samir et al., 1990; Thomas et al., 2002; Soulaimani et al., 2003), and includes Lower Cambrian carbonates, siltstones, and marls as well as Middle Cambrian to Middle Devonian sandstones and shales. These strata were subsequently deformed during the Variscan orogeny and unconformably covered by marine (mainly Cretaceous) sediments (Figure 1a). The eastern Anti-Atlas includes another elevated (~2700 m) volcanic field, the Saghro Massif. (Figure 1a). This is composed of multiple late Miocene tuff cones which, likewise the Siroua Massif, overlie a wide erosional surface sculptured on the Precambrian basement.

1. **Geophysical and petrological data**

The peculiarity of the Atlas-Meseta orographic system is the lack of orogenic roots generated through crustal shortening and thickening processes that would isostatically support the modern topography. This applies to the HA (Beauchamp et al., 1999; Gomez et al., 2000; Teixell et al., 2003; Domènech et al., 2016; Fekkak et al., 2018; Lanari et al., 2020b) and the MA (Gomez et al., 1998; Arboleya et al., 2004; Pastor et al., 2015), where tectonic shortening has occurred during the Cenozoic, and to the tectonically inactive AA, Western and Eastern Meseta (Babault et al., 2008; Frizon de Lamotte et al., 2009; Pastor et al., 2015). Several geophysical and petrological studies indicate an anomalous thinning of the lithosphere with a shallow, hot asthenosphere beneath the entire Atlas-Meseta orographic system (El Azzouzi et al., 1999; Missenard et al., 2006; Duggen et al., 2009; Miller et al., 2015). This includes geophysical modelling of gravity data, S-received function (Ayarza et al., 2005; Missenard et al., 2006; Miller and Becker, 2014; Miller et al., 2015), heat flow measurements, deep electrical resistivity (Rimi et al., 1999; Zeyen et al., 2005) and seismic tomography (Seber et al., 1996; Palomeras et al., 2014; Bezada et al., 2014). The shallow asthenosphere is thought to support the present-day topography of the Atlas-Meseta system, which should have been generated, at least in part, by deep-seated, mantle driven processes. For example, a maximum of 2000 m of residual topography has been estimated in the HA and MA considering a crustal thickness of ca. 35 km (Miller and Becker, 2014), while more than 1000 m of elevation has been attributed to dynamic topography (Frizon de Lamotte et al., 2009; Spieker et al., 2014).

Magmatic activity in the Siroua, Saghro and the MA Mountains presents an alkaline affinity indicating a partial melting of sublithospheric mantle caused by heating generated by asthenospheric flow (El Azzouzi et al., 1999; 2010; De Beer et al., 2000; Missenard et al., 2006). The geochemical signature and trace element patterns of the MA lavas are very similar to those observed in the Canary Islands, suggesting a possible link between the Canary mantle plume and continental intraplate volcanism in the Atlas-Meseta system (Duggen et al., 2009). Interestingly, magmatism occurred in two different pulses, in the Eocene and middle-late Miocene in association with renewed tectonic activity. A more recent phase of magmatism, however, has occurred in the MA and Western Meseta during the last 2 Ma, apparently without major acceleration in tectonic deformation (El Azzouzi et al., 2010; Missenard et al., 2012).

1. **Methods**

3.1. River profiles, knickpoints discretization and celerity model

River networks represent a powerful reconnaissance tool to investigate the impact of rock uplift and climate changes on landscape evolution (Hack, 1957; Kirby and Whipple, 2001; Wobus et al., 2006; Kirby and Whipple, 2012; Whittaker, 2012). This is possible because channel steepness and erosion rates along river profiles adjust to rock uplift, climatic conditions, and bedrock erodibility (Duvall et al., 2004; DiBiase and Whipple, 2011). Channel slopes along the stream commonly exhibit an inverse power-law scaling relationship with upstream contributing drainage area (Flint, 1974). Hence, the stream power model describes the variation of channel elevation in time (*dz/dt*) (Howard and Kerby, 1993; Whipple and Tucker, 1999):

$\frac{\mathrm{dz}}{\mathrm{dt}} = U - KA^m S^n$ (1)

where U is the rock uplift rate, K is the fluvial erodibility coefficient controlled by bedrock lithology, climate and sediment load, A is the upstream drainage area, S is the local channel slope and m and n are constants that depend on basin hydrology, channel geometry and erosional processes (Howard, 1994; Whipple and Tucker, 1999). Under steady state conditions erosion and rock uplift rates (U) are balanced (Willett and Brandon, 2002; Kirby and Whipple, 2012), and there is no change in elevation of the channel bed over time ($dz/dt = 0$). Therefore, equation (1) can be rearranged as:

$$S = \left(\frac{U}{K}\right)^{\frac{1}{n}} A^{-\left(\frac{m}{n}\right)} \quad (2)$$

where $(U/K)^{1/n}$ and m/n are the channel steepness index (*ks*) is the concavity index ( ), respectively (Flint, 1974). The relationship in equation (2) is only valid above a critical upstream drainage area of 0.1 to 5 km^2, where fluvial processes dominate over debris flow processes (Montgomery and Foufoula, 1993; Stock and Dietrich, 2003; Wobus et al., 2006). Channel steepness and concavity indices can be extracted from DEMs by a logarithmic regression of the local channel slope versus the contributing drainage area (Whipple, 2004; Wobus et al., 2006) or through an integral approach (Perron and Royden, 2013). To allow the effective comparison among longitudinal profiles with greatly varying drainage areas and counteract the influence of DEM-noise, we used a typical reference concavity index ($_{ref}$) of 0.45. This allowed to calculate the normalized channel steepness index (k_{sn}), a parameter which is sensitive to variations in bedrock erodibility, climate conditions and rock uplift (Snyder et al., 2000; Wobus et al., 2006). The chosen $_{ref}$ value falls in the range of estimates upstream and downstream of non-lithological knickpoints of the Anti-Atlas, as discussed in Clementucci et al. (2022).

Furthermore, we performed a regional scale topographic and statistical analyses, using the integral approach calculating along the main river segments. A linear regression though allows estimating and k_{sn} (Clementucci et al., 2022). These results are comparable with values estimated from the log slope-log area method of the same river network (Tables S1, S2 and Figure S3 in supporting information). Importantly, the integral approach allows visualizing k_{sn} variation along the stream segments and to discretize the knickpoints. The method is based on the transformation of the horizontal coordinates of a river profile to the reference frame assuming steady state conditions and spatially invariant uplift rates and bedrock erodibility (Perron and Royden, 2013):

$$z(x) = z\left(x_b\right) + \left(\frac{U}{KA_0^m}\right)^{\frac{1}{n}} \int_{\mathrm{xb}}^{x} \left(\frac{A_0}{A(x)}\right)^{\frac{m}{n}} \mathrm{dx} = z\left(x_b\right) + k_s\ A_0^{-\left(\frac{m}{n}\right)} \chi \quad (3)$$

$$= \int_{\mathrm{xb}}^{x} \left(\frac{A_0}{A(x')}\right)^{\frac{m}{n}} \mathrm{dx} \tag{4}$$

where is the independent variable of integral quantity in the upstream direction from a base level x_b to an observation point x, z is the elevation along the channel, ks (or k_{sn} assuming a reference concavity) is the steepness index and A_0 is the reference drainage area, usually assumed to be 1 km^2 (Perron and Royden, 2013). In the $-z$ plot the slope is proportional to the normalized channel steepness index (k_{sn}). In areas where erodibility and climate variability are marginal, the river network analysis can be used to infer and visualize the pattern of relative rock uplift rate across the region. Usually, a variation in rock uplift rate is identified by the presence of "transient knickpoints" which separate portions of the landscape eroding at different rates (Kirby and Whipple, 2012; Royden and Perron, 2013; Mudd et al., 2014). A detailed analysis of these features is fundamental to understand the state of a landscape. Distinguishing the nature of the knickpoints requires a detailed analysis of the geological and geomorphic characteristics (Kirby and Whipple, 2012). Transient and lithological knickpoints were differentiated by looking at: (1) their position and distribution in the $-z$ plot (*i.e.*, rivers that experienced a similar rock uplift history should cluster in the $-z$ plot; Gallen and Wegmann, 2017; Figure S2 in supporting information); (2) available geological maps (1: 200.000, 100.000 and 50.000, Service Géologique du Maroc); and (3) satellite imagery on Google Earth (further details in section S1 in supporting information).

Subsequently, a celerity model was applied to calculate the onset of knickpoints migration. By using the stream model shown in equation (1), considering plucking as the primary erosion mechanism ($n = 1$). The horizontal migration of knickpoints along the river profiles in response to a relative base-level drop can be described as:

$$\frac{\mathrm{dx}}{\mathrm{dt}} = KA^m \ (5)$$

where, *dx/ dt* is the knickpoint celerity, K is a dimensional coefficient of erosion (Whipple and Tucker, 1999; Whipple, 2004), A is upstream drainage area and m is a non-dimensional parameter that depends on basin hydrology, channel geometry, and erosion process (Whipple and Tucker, 1999). In our case, m was allowed to vary linearly between 0 and 0.75, as suggested by the present-day topography (Tables S1, S2 and Figure S3 in supporting information), while K was allowed to vary between 10^{-7} and 10^{-4} (Figure S5), in agreement with the relationship between ^{10}Be denudation rates and k_{sn}, using a linear version of the stream power model (Clementucci et al., 2022). Finally, we set the onset of knickpoints migration between 3.8 and 18.6 Ma (details in section S1 and 4.4). This timing was estimated by using the maximum excavation time required to erode the missing rock volume from the river catchments (Table S4).

A Shuttle Radar Topography Mission Digital Elevation Model (SRTM DEM, pixel size of 90 m) was used to perform the topographic and the river network analysis described above. All steps were conducted using ArcGIS tools, Topo-

Toolbox (Schwanghart and Scherler, 2014), TAK (Forte and Whipple, 2019) and a series of MATLAB functions (Gallen, 2017; Smith et al., 2022).

1. **River projections**

The magnitude of fluvial incision, associated with changes in rock uplift, can be estimated from the relict topography upstream of major non-lithological knickpoints (Berlin and Anderson, 2007; Schildgen et al., 2012; Gallen et al., 2013; Miller et al., 2013). In particular, the reconstructed river projection from the relict landscape allows determining the paleo-base level and hence the magnitude of minimum incision/surface uplift and paleo-relief before the development of the knickpoints (Olivetti et al., 2016; Heidarzadeh et al., 2017; Fox et al., 2019). Particularly, the estimates represent the incision into a specific surface which may be undergoing continued erosion itself. Therefore, incision may not represent total erosion but the difference between the erosion across the low-relief landscape and that within the incising part of the landscape. We carry out two types of river projections: one dimensional projections where the elevation only varies as function of distance along a single channel and the model parameters are single values of surface uplift and paleo-channel steepness; two dimensional projections where elevation varies as a function of space and the model parameters are maps of surface uplift and paleo-channel steepness. One dimensional projections were carried out in   space with $_{\mathrm{ref}} = 0.45$. To do this a linear model was regressed through the -elevation data from the relict part of the landscape. The intercept with y axis (i.e., where =0) provides the elevation of the paleo-baselevel. This approach relies on several assumptions: that the paleo-river network has remained approximately the same through time; erosion rates across the relict landscape have remained constant; the channel steepness in the paleo-landscape was spatially uniform; and that the change in baselevel due to surface uplift is spatially uniform. The assumption that the erosion rates have remained overall steady across the Anti-Atlas relict landscape is justified by the close match between short and long-term erosion rates throughout the Cenozoic (*i.e.*, erosional steady-state; *e.g.*, Willett and Brandon, 2002; Clementucci et al., 2022). However, there is no guarantee that the projected rivers within the same catchment will predict the same amount of surface uplift. This has the benefit of providing a test of the underlying assumptions, however, the resulting landscape may be unrealistic because predicted elevations at confluences may be different.

A two dimensional approach, proposed by Fox (2019), allows reconstructing the paleo-topography ensuring tributaries and trunk streams share the same elevation at confluences. This approach was extended by Fox et al., (2020) and Smith et al., (2022) to account for spatial variability in surface uplift. The basis of this approach is that a discrete version of the stream power model can be written using a series of nodes along the main trunk river:

$$\mathrm{z}_{\ i} - B.L. \ = \ \sum_{j=1}^{i} \left(\Delta\chi_j\right) u_j^* + \mathrm{S.U.}_{\cdot i} \quad (6)$$

where the *i*th pixel is the upstream of the *j*th pixel and the lowest most pixel has the elevation of B.L. (baselevel), $S.U.i$ is the surface uplift that the relict landscape has experienced following fluvial dissection, $u*$ is the normalized rock uplift rate, which is proportional to the normalized channel steepness that is preserved across the relict landscape. This expression provides a prediction of elevation as a function of channel steepness and surface uplift. Provided both vary smoothly in space over long length scales, the elevation of pixels within the DEM can be used to recover these values using inverse methods. The results provide a reconstructed pre-incision landscape and allows quantifying the amount of surface uplift for each node (Smith et al., 2022). Maps of $u*$ and $S.U.$ can be calculated to minimize the misfit between predicted and observed topography of the relict landscape and the roughness of the $u*$ and $S.U.$ maps. In this case, the values were calculated for the entire drainage network of the Anti-Atlas but only the upstream knickpoints on the relict landscape were used to estimate the $u*$ and $S.U.$. We used values of $m = 0.45$, $A_0 = 1$ m^2. Because the topographic reconstruction requires many more model parameters, smoothness constraints in the form of weighted negative Laplacian operators are required. We used weighting parameters for the S.U. parameters and $u*$ (and , respectively) equal to 10 and the grid size to 5 km, for the inversion method. The main assumptions of the method are that the shape of the river network has remained constant in time, there was no major drainage reorganization, and the erodibility coefficient (K) is considered constant.

1. **Results**

   (a) **Topographic analysis**

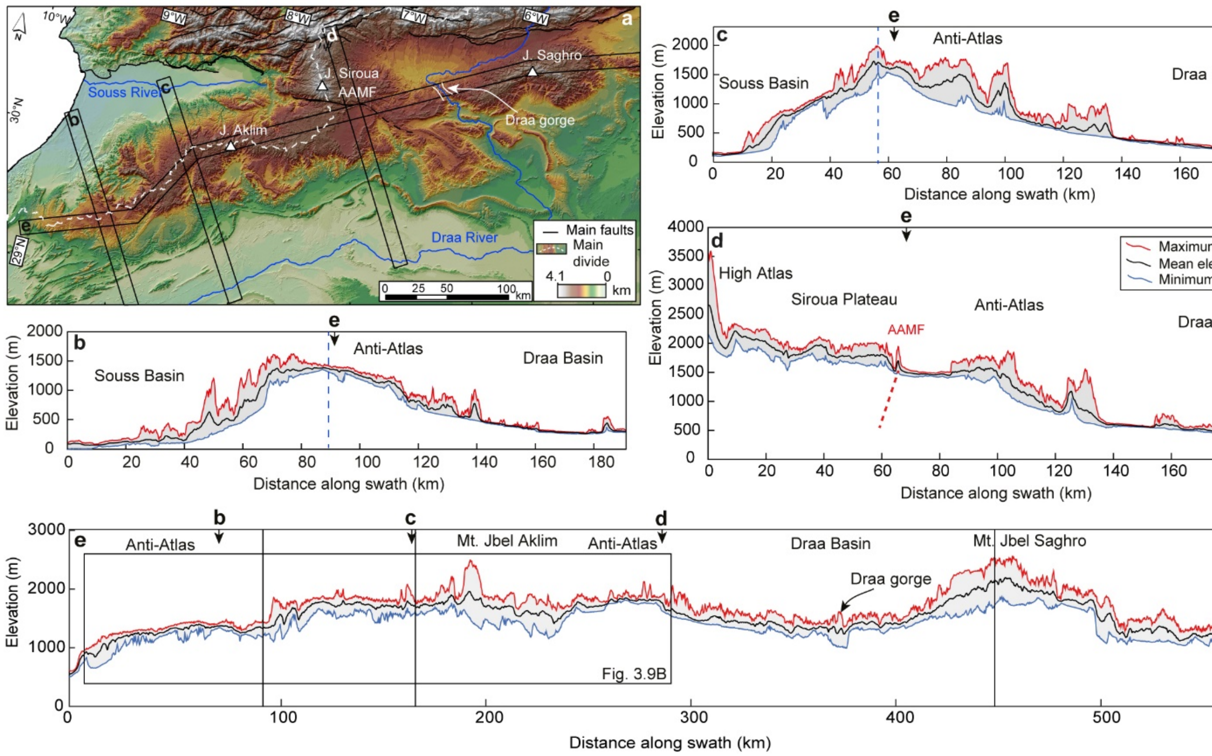

Figure 2. (a) Topographic map of the Anti-Atlas and the Siroua Massif (SRTM DEM database) with location of the swath profiles. The dashed white line indicates the position of the main drainage divide. (b, c, d) are swath profiles orthogonal to the main drainage divide of the Anti-Atlas, while (e) is parallel to the main drainage divide. The dashed blue line indicates the position of main drainage divide on swath profiles b, c.

The AA is characterized by an extensive, high-standing (~2000 m), axial zone with low-topographic relief delimited by steep and dissected flanks (Figure 2). The westernmost sectors of the belt have a dome-shape geometry with a rather symmetric topography across the drainage divide (Figure 2b). The central sectors of the western AA have an asymmetric topography with a gentle southern and a steep northern flank grading toward the Draa and the Souss basins, respectively (Figure 2c). The central AA has also a flat top but is bounded to the north by the Siroua plateau through a topographic step in proximity of the Anti-Atlas Major Fault (AAMF; Figure 2d). The along-strike swath profile highlights the geometry and the extent of the elevated axial surface, with a few mountain peaks (*e.g.*, Mt. Jebel Aklim, 2531 m and Mt. Jebel Saghro, 2592 m) and deeply incised valley (the Draa gorge; Figure 2a and 2e). The high-standing landscape is mostly composed of Paleozoic limestones and Precambrian basement rocks (Figure 3a) and is located upstream of non-lithological knickpoints. Downstream of these knickpoints, the topography is steeper and includes late Precambrian and Paleozoic sedimentary rocks (Figure 3). The northern flank of the belt has a slope that is sub-parallel to the bedding of late Precambrian carbonates and consists of narrow and deep valleys perpendicular to the bedding (Figure 4, profile a-a'). Conversely, the southern flank includes wide valleys mostly located along the core of the synclines with Paleozoic sediments (Soulaimani and Burkhard, 2008; Figure 4, profile b-b'). Finally, the swath profiles indicate that the high-standing, elevated surface plunges along the strike of the mountain belt (Figure 2e), and perpendicularly to it (Figure 2b, 2c).

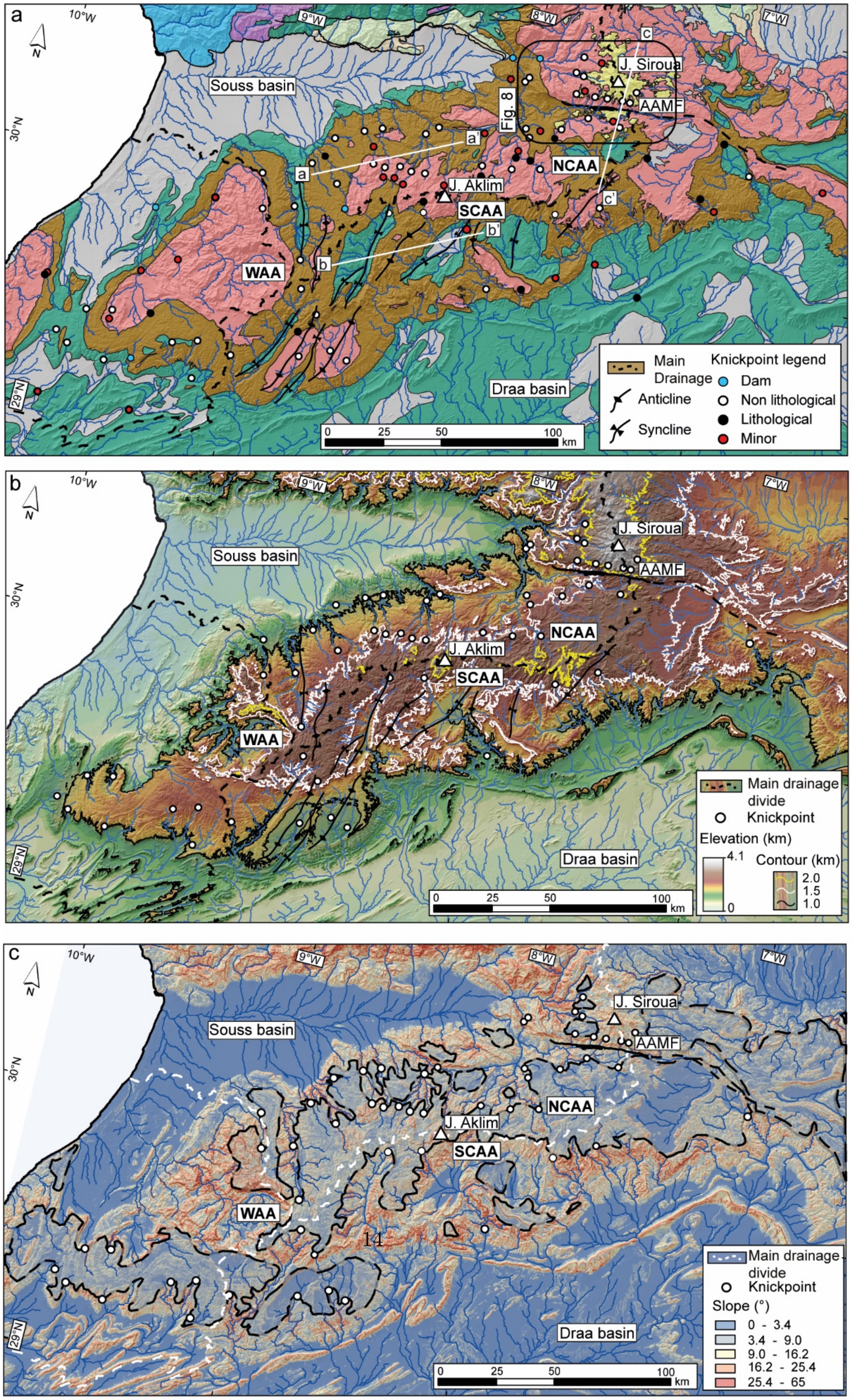
a
10°W
9°W
8°W
7°W
30°N
29°N
N
Souss basin
J. Siroua
AAMF
Fig. 8
c
c'
a
a'
b
b'
J. Aklim
NCAA
SCAA
WAA
Draa basin
Main Drainage
Anticline
Syncline
Knickpoint legend
Dam
Non lithological
Lithological
Minor
0
25
50
100
km
b
10°W
9°W
8°W
7°W
30°N
29°N
N
Souss basin
J. Siroua
AAMF
J. Aklim
NCAA
SCAA
WAA
Draa basin
Main drainage divide
Knickpoint
Elevation (km)
4.1
0
Contour (km)
2.0
1.5
1.0
0
25
50
100
km
c
10°W
9°W
8°W
7°W
30°N
29°N
N
Souss basin
J. Siroua
AAMF
J. Aklim
NCAA
SCAA
WAA
Draa basin
Main drainage divide
Knickpoint
Slope (°)
0 - 3.4
3.4 - 9.0
9.0 - 16.2
16.2 - 25.4
25.4 - 65
0
25
50
100
km

Figure 3. (a) Geological map of the study area with a detailed analysis of the knickpoints for the northern flank of the central Anti-Atlas (NCAA), western (WAA), and southern flank of central Anti-Atlas (SCAA) and the Siroua Massif. The main fold axes are associated with the Variscan orogeny and are shown with black lines (from Soulaimani and Burkhard, 2008). (b) Topographic map (SRTM DEM database) of the study area with the non-lithological knickpoints and the fold axes. The black, white and yellow dashed lines demark the 1000, 1500 and 2000 m contours, respectively. (c) Slope map of the study area with non-lithological knickpoints. The dashed line indicates the low-slope area of the axial zone of the Anti-Atlas (after Clementucci et al., 2022). Location of the maps is shown in figure 1b.

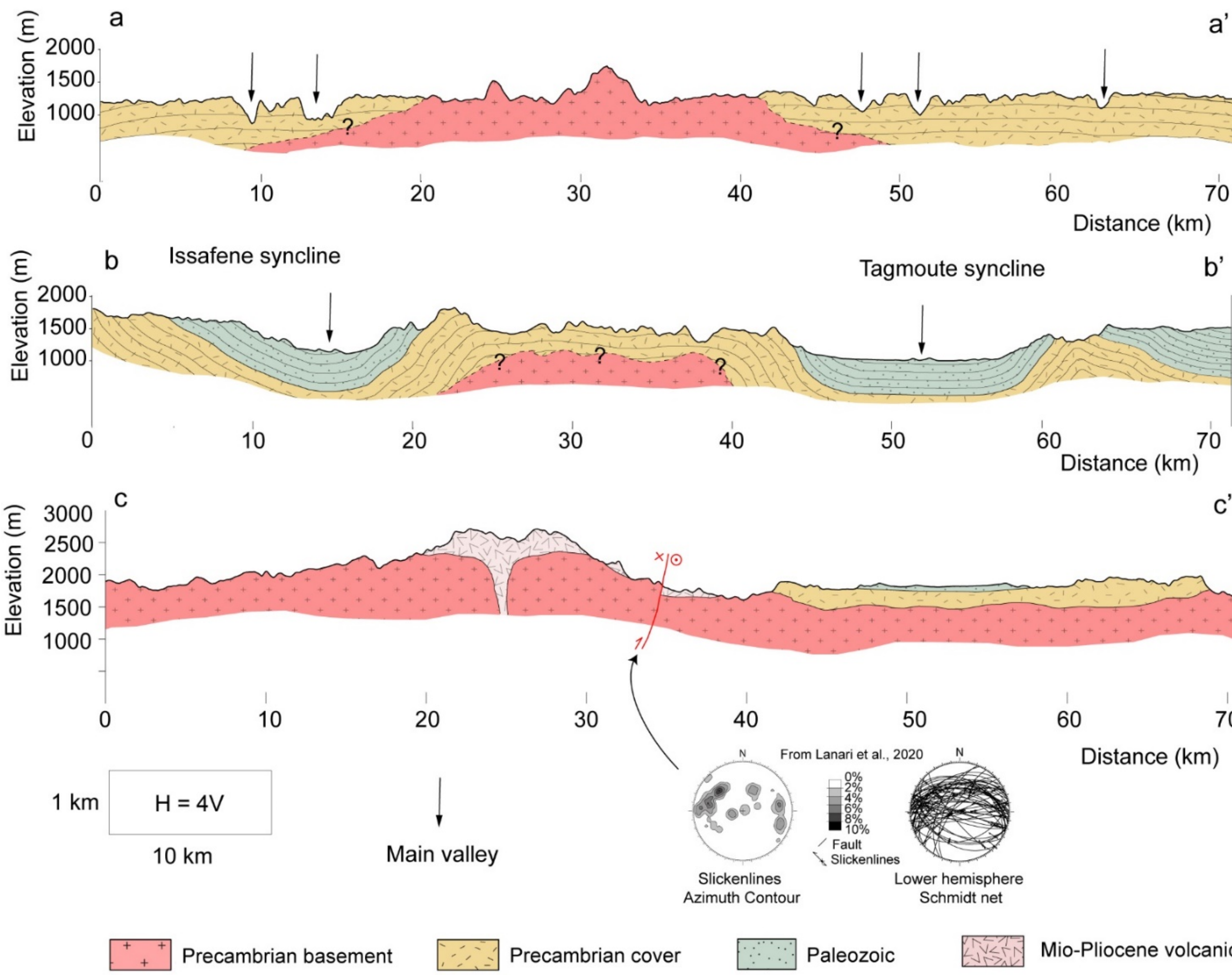

Figure 4. a-a' geological cross section of the northern flank of the Anti-Atlas. b-b' geological cross section of the southern flank of Anti-Atlas. c-c' geological

cross section in the Siroua Massif. Location of the cross-sections is indicated in figure 3a.

4.2 River morphology

Seventeen stream profiles from the northern flank of the central Anti-Atlas (NCAA) together with seventeen profiles from its southern flank (SCAA) and fourteen from the western side of the orogen (WAA) were analysed individually. Specifically, we extracted the main knickpoints, the concavity values ( ) and the normalized channel steepness indices (k_{sn}) for the main river trunks using the log S-log A approach and the integral method. In the AA, most of the rivers are characterized by transient conditions with mean k_{sn} values of 84 ± 3.8 (= 19.7) $m^{0.9}$ and 30 ± 2.9 (= 14.8) $m^{0.9}$, and values of 0.58 ± 0.04 (= 0.22) and 0.17 ± 0.03 (= 0.18) in the downstream and the upstream segments, respectively (detailed analysis of k_{sn} and is shown in Table 1 and Table S1).

Table 1

Summary the river profile data of k_{sn} and upstream and downstream of non-lithological knickpoints (details in Table S1).

Sector	Stream parameters				
	Downstream	Upstream			
	ksn ($m^{0.9}$)		ksn ($m^{0.9}$)		
NCAA[a]	mean[d]	102.6 ± 4.7	0.44 ± 0.02	33.2 ± 3.5	0.18 ± 0.04
	[e]	14.8	0.07	11.1	0.14
SCAA[b]	mean	82.2 ± 2.7	0.57 ± 0.03	22.7 ± 5.1	0.17 ± 0.07
		7.2	0.09	13.5	0.2
WAA[c]	mean	65.07 ± 3.1	0.75 ± 0.1	33.23 ± 6.1	0.14 +. 0.07
		9.45	0.3	18.5	0.22
Tot	mean	84.1 ± 3.8	0.58 ± 0.04	30.4 ± 2.9	0.17 ± 0.03
		19.7	0.22	14.8	0.18

Note. [a] NCAA : rivers draining the northern flank of Anti-Atlas. [b] SCAA : rivers draining the southern flank of Anti-Atlas. [c] WAA : rivers draining the western flank of Anti-Atlas. [d] Mean and standard error values. [e] Standard deviation of the data.

The NCAA is mostly characterized by transient longitudinal river profiles. Overall, we recognized 51 knickpoints with two main patterns of non-lithological knickpoints standing between 700 and 1000 m and 1300 and 1500 m of elevation and several minor lithological knickpoints (Figures 3a, 3b and 5a). The two patterns of non-lithological knickpoints cluster approximately at values of of 3-5 and 9–11, respectively (Figure 5b). The steepest and concave up segments of the NCAA rivers are downstream of the highest knickpoints (Figure 5a, 5b), whereas, the upstream segments are mostly rectilinear, have a shallow gradient and contain minor knickpoints (Figures 3a and 5a, 5b). Another minor group of knickpoints separating gentle upstream river segments from steeper downstream portions is in the Siroua Massif, over 2000 m of elevation (see red profiles in figure 5a and 5b), upstream of the Anti-Atlas Major Fault (AAMF, Figure 6).

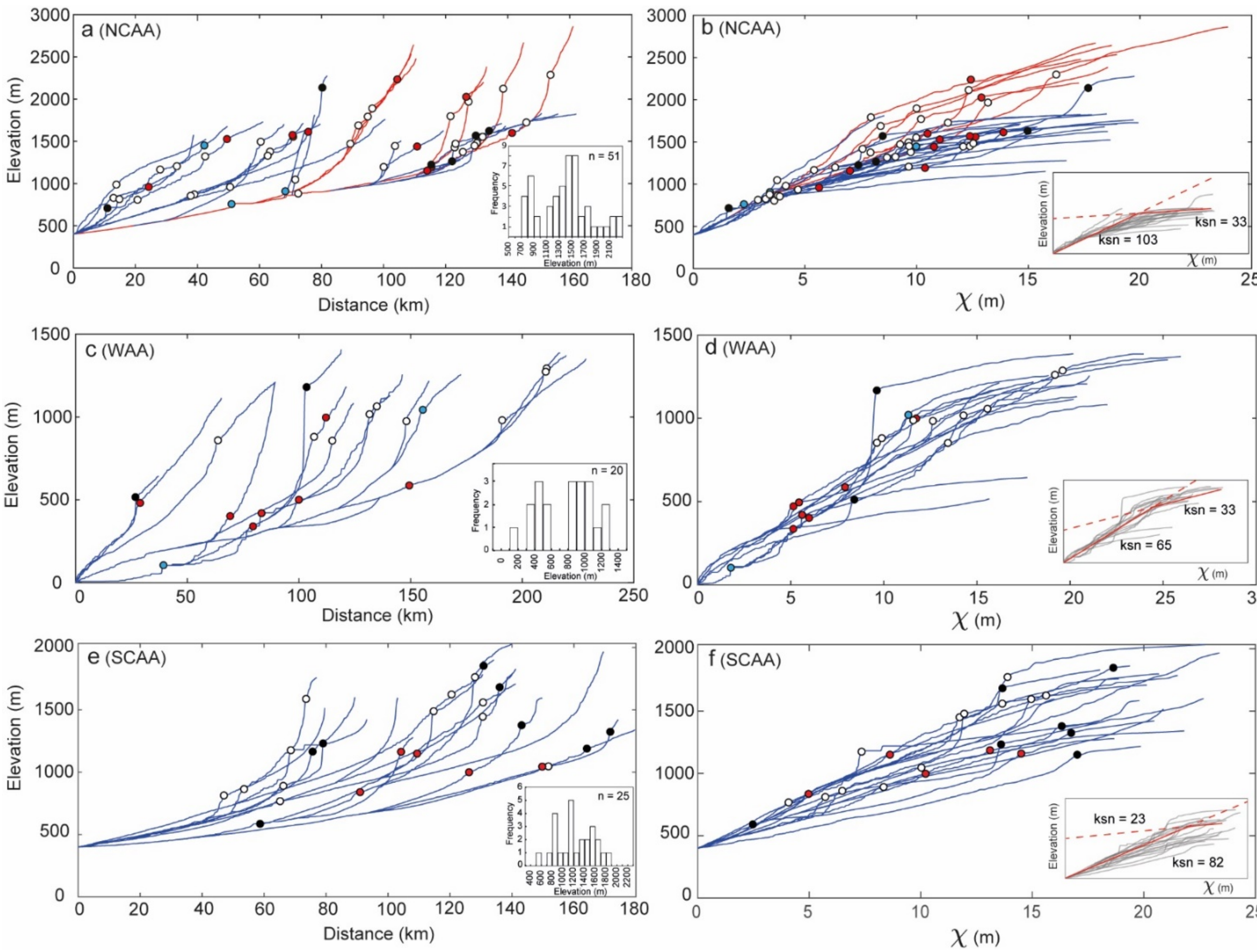

Figure 5. Longitudinal river profiles and   plots with major knickpoints for (a-b) NCAA, (c-d) WAA, and (e-f) SCAA. The rivers of NCAA and SCAA sectors are extracted from the bedrock-alluvial transition, which in the study area is around 400 m. The knickpoints legend is in figure 3a. The red profiles indicate the rivers flowing from the Siroua Massif. The inset plots in the   space show the mean regional k_{sn} values upstream and downstream of the highest knickpoints. The inset histogram in the longitudinal profiles show the frequency distribution of the elevation of the knickpoints.

The WAA sector presents also transient river profiles with approximately 20 knickpoints. Most of the non-lithological knickpoints are located within a relatively narrow elevation band, of about 800 to 1100 m while the minor knickpoints are at about 400 to 500 m (Figure 5c, 5d). The steeper downstream portion of the major non-lithological knickpoints exhibit a concave-up geometry with a few minor knickpoints (Figure 5c, 5d). The upstream segments are mostly rectilinear with a typical equilibrium profile (straight segment in space; Figure 5d). Here, the two patterns of knickpoints at ~500 m and ~1000 m, occur approximately at values of 5-6 and 10–15, respectively (Figure 5d).

The SCAA sector is characterized by both, equilibrated and transient longitudinal river profiles and contain at least 25 knickpoints distributed across a wide range of elevation (Figure 5e). Most of the non-lithological knickpoints stand at about 800 to 1000 m of elevation and over 1500 m of elevation, while the lithological knickpoints are at an elevation range of 1000 to 1500 m (Figure 5e, 5f).

The k_{sn} and values obtained with the logS-logA method were compared with those estimated with the method (Clementucci et al., 2022; Tables S1 and S2 in the supporting information). k_{sn} values lie mostly on the 1:1 trend (Figure S3a), while the values show a higher dispersion (Figure S3b in the supporting information). Finally, the elevation and distance from the river mouth show a positive correlation with the drainage area of catchments (Figure S4b and S4c).

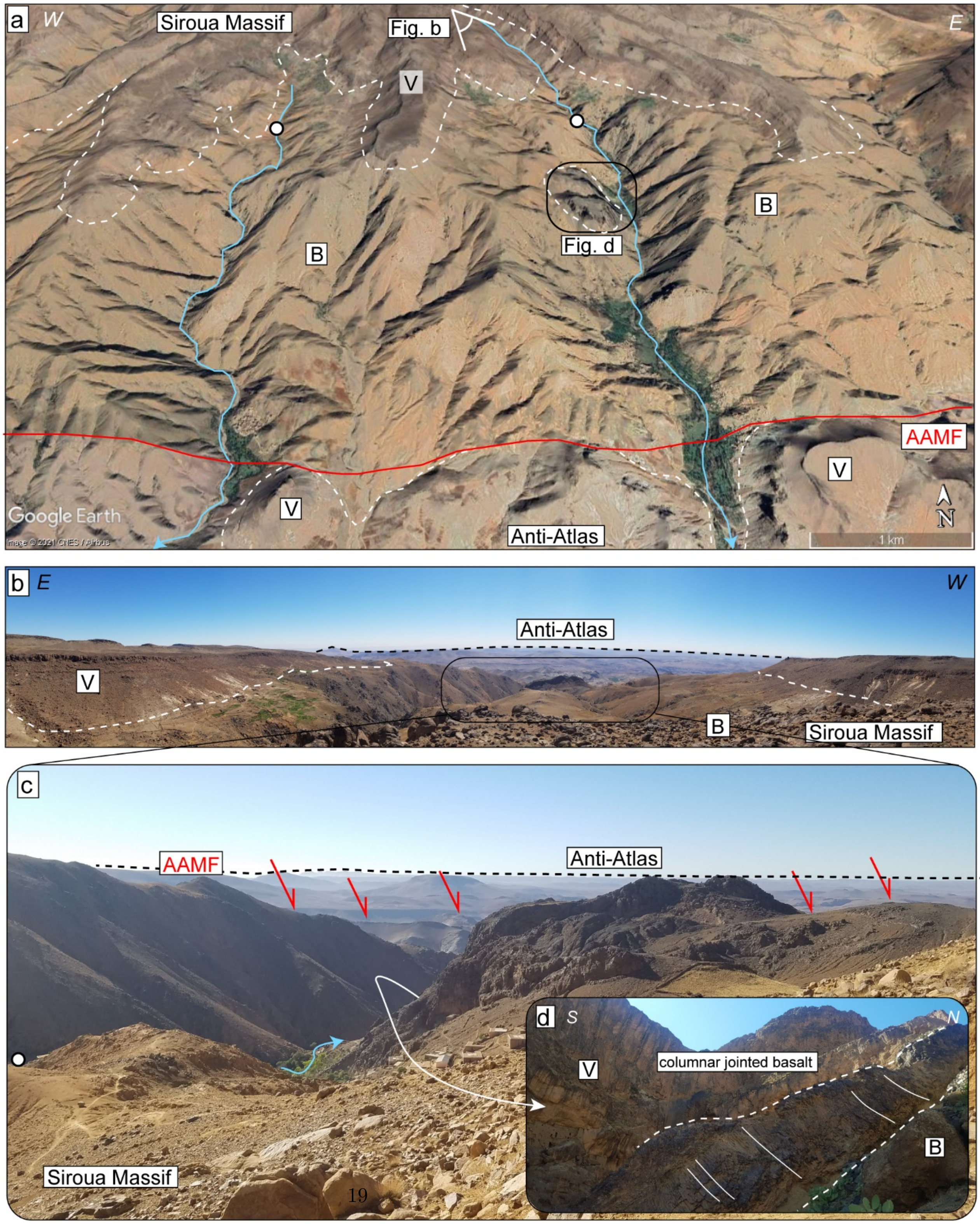
a
W
Siroua Massif
Fig. b
V
E
B
Fig. d
B
AAMF
V
V
Google Earth
Anti-Atlas
N
1 km
b
E
W
Anti-Atlas
V
B
Siroua Massif
c
AAMF
Anti-Atlas
Siroua Massif
d
S
N
V
columnar jointed basalt
B

Figure 6. (a) Prospective Google Earth view of the southern flank of the Siroua Massif. Note the volcanic edifice composed of lava flows demarked by the dashed white line (see V symbol) resting unconformably over the Precambrian basement (see B symbol), the north-dipping Anti-Atlas Major Fault (AAMF), the non-lithological knickpoints shown with a white dot, the deep incisions and the remanence of the lava flows downstream of the non-lithological knickpoints. (b) Panoramic view from the Siroua Massif showing in the background the summit erosional surface (i.e., relict landscape) of the Anti-Atlas (see dashed black line) and in the foreground the contact between the basement (B) and the lava flows (V). (c) Detail of figure 6b showing the basalt flow preserved in the deeply incised valley of figure 6a. (d) Field picture of the basalt of figure 6c with high angle columnar joint (white lines) perpendicular to the valley bottom (dashed white lines).

4.3 Magnitude of fluvial incision

1. **1D river projection**

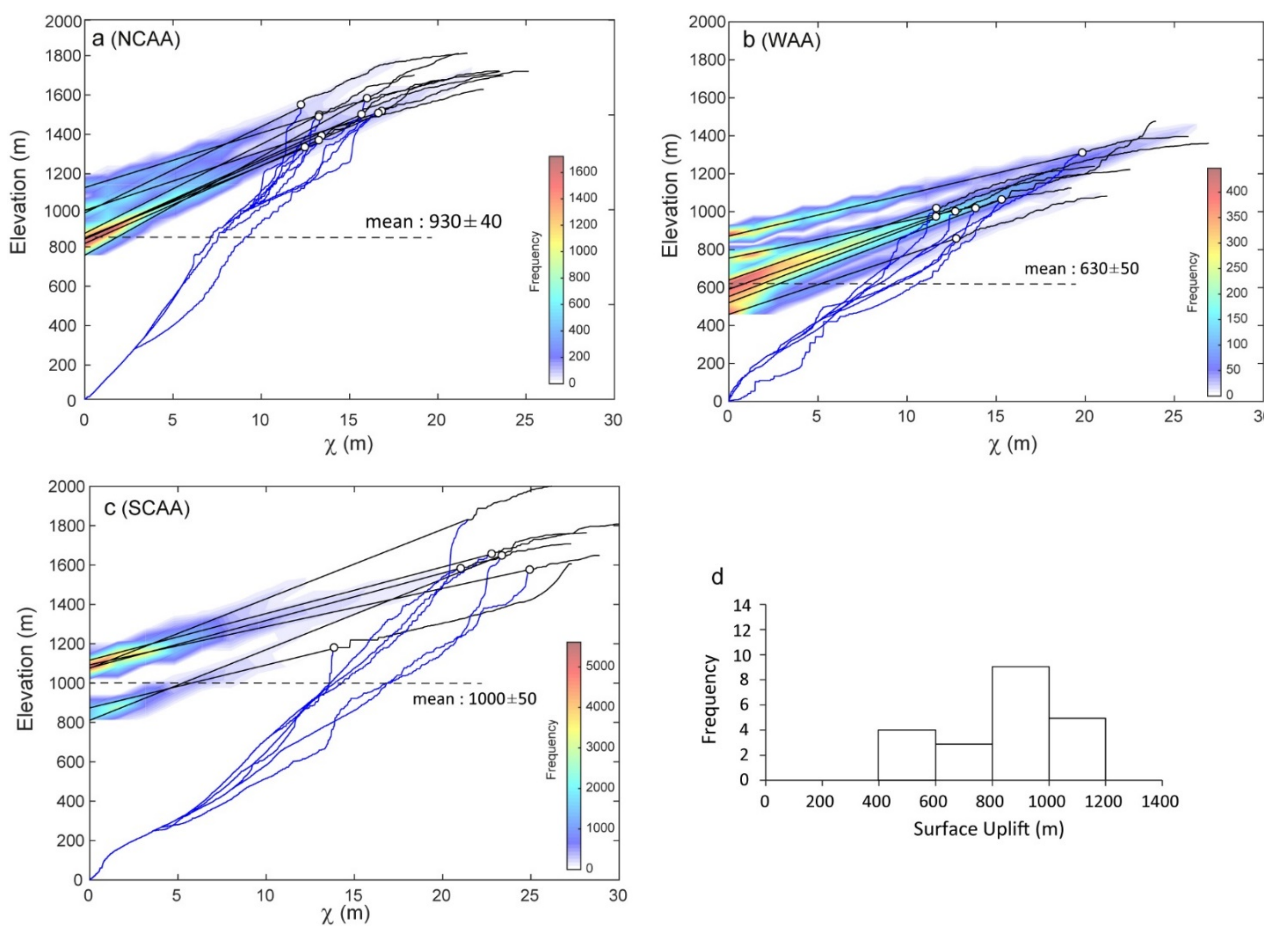

Figure 7. Modern longitudinal profiles and projections of the relict landscape (red segments) upstream of the highest knickpoints using $_{ref} = 0.45$ and the k_{sn} of the relict portion for the (a) NCAA, (b) WAA, and (c) SCAA sectors. Major knickpoints are marked with white circles. (d) Frequency diagrams of the magnitude of surface uplift for the different sectors.

The Souss and Draa outlets represent the present-day base level for the NCAA and SCAA rivers, respectively, whereas the WAA rivers flow directly into the Atlantic Ocean. To a first approximation we can consider that all rivers of the Anti-Atlas drained toward the Atlantic before the relative base level fall that initialized the most elevated non-lithological knickpoints (Figure 5). This because the opening of the South Atlantic Ocean had already occurred in the early Cretaceous (Torsviket al., 2009) and hence much earlier than the Cenozoic topographic rejuvenation. Estimated values of fluvial incision for the NCAA based on 10 stream profiles range from 822 (2 = 36) to 1162 m (2 = 18), with an average of 930 ± 42 m (= 133) (Figure 7 and Table S3). In the WAA sectors, 7 transient profiles yielded fluvial incision values ranging from 459 (2 = 9) to 872 m (2 = 29), with an average of 630 ± 54 m (= 143) (Figure 7 and Table S3). Finally, in the SCAA where most of the rivers are in equilibrium, the fluvial incision based on 6 stream profiles ranges from 811 (2 = 117) to 1117 m (2 = 18), with an average of 1008 ± 53 m (= 130) (Figure 7 and Table S3). Furthermore, this approach allows estimating the first-order paleo-topographic relief as the difference between the modern mean drainage divide elevation and the elevation of the outlet of the reconstructed river profiles. Our results indicate a mean elevation difference of 970, 890 and 750 m for the NCAA, SCAA, and WAA sectors, respectively (Table S3 in the supporting information).

In the Siroua Massif, rivers are characterized by strong disequilibrium profiles with high-standing non-lithological knickpoints lying at the margin of a low-topographic relief area and delimiting streams with high k_{sn} from those with low k_{sn} values (Figures 6a, 8a, 8b). The magnitude of fluvial incision along the Siroua escarpment was obtained by projecting the upstream portions of the rivers up to the AAMF (Figure 8c, 8d). This value is ~350 m and represents only the amount of incision between the Siroua Massif and the central sector of AA.

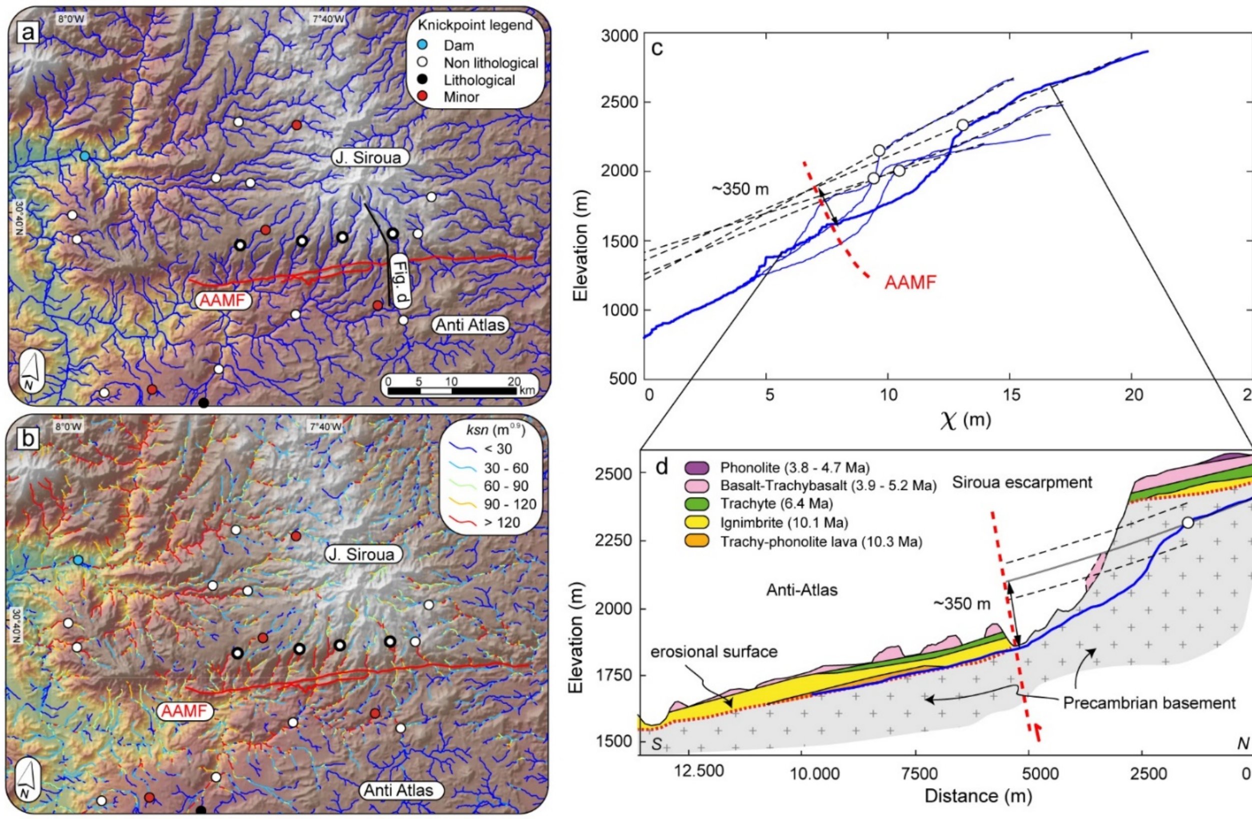

Figure 8. (a)Topographic map (SRTM DEM database) of study area with the main knickpoints. Bold blue rivers and associated knickpoints (thick black circles) are projected in figure 8c. (b) k_{sn} map of the stream network in the Siroua area. Location of the maps is shown in figure 3A. (c) Modern longitudinal profiles and projections from the Siroua relict landscape (dashed black segments) upstream of the highest knickpoints using $_{ref} = 0.45$ and the k_{sn} of the relict portion. Note, the reconstructed river projections intersect each other between 5 and 10 of . (d) Geological profile of the Siroua escarpment (after De Beer et al., 2000). The minimum value of incision is 350 m.

Overall, our projections document a progressive increase in the magnitude of fluvial incision and in the elevation of the highest knickpoints from the WAA to the central sector of AA with a culmination in the Siroua Massif (Figure 9b). This is also associated with a regional increase in k_{sn} values downstream of the major knickpoints (red dots in figure 9a).

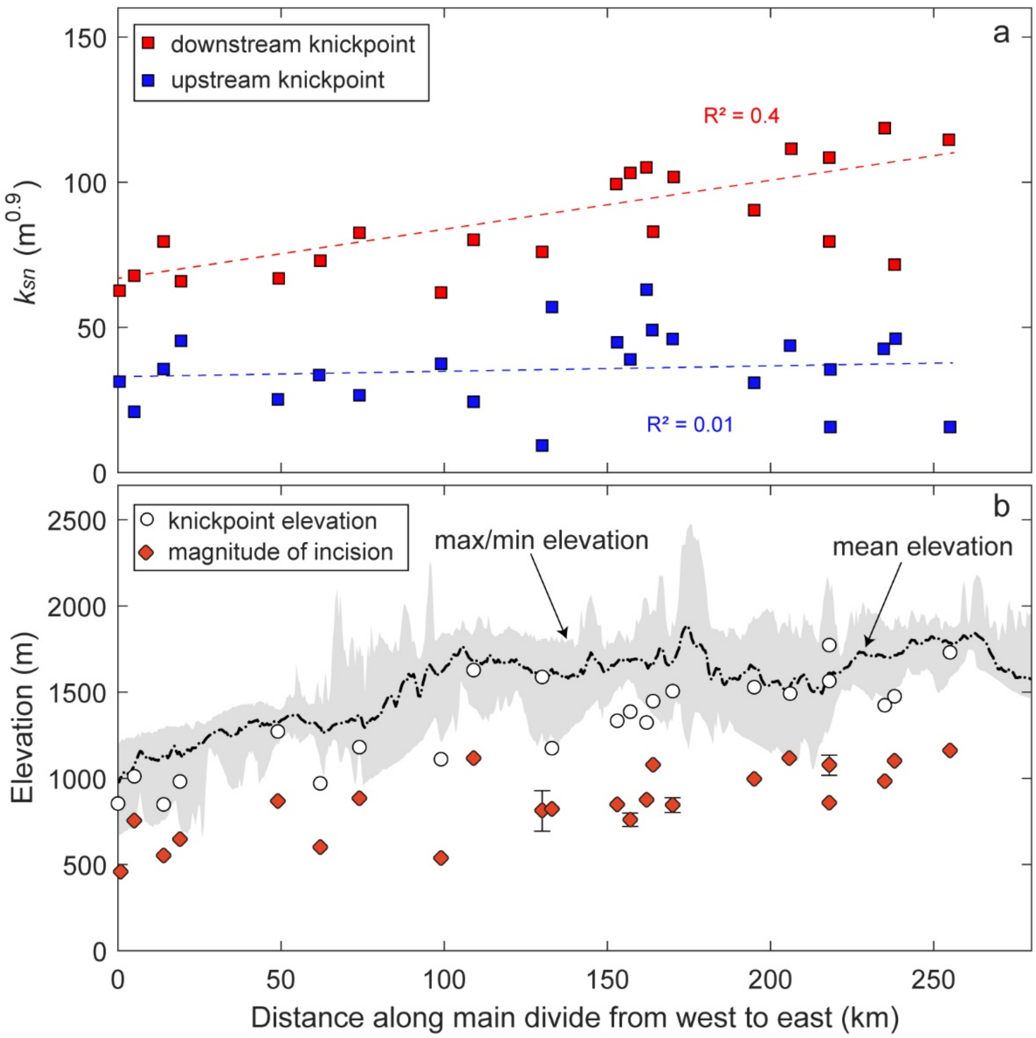

Figure 9. (a) Distance along the main drainage divide versus k_{sn} down and upstream of the non-lithological knickpoints. (b) Distance along the main drainage divide versus knickpoint elevation and estimated surface uplift values. The location of the swath profile is indicated in figure 2d.

1. **2D river projection**

The 2D river projection method allows estimating the distribution of surface uplift (or baselevel fall) and normalized rock uplift rates, $u*$ proportional to k_{sn}, as a function of the elevations and the values from the relict river network (in the portion of landscape demarks by white polygon in figures 3c and S6). Due to the increased spatial variability provided by this approach, multiple solutions which pass through the and elevation data are expected, and results are non-unique. Damping forces smooth maps providing a means to choose a preferred result. Here damping parameters are chosen to ensure that results are consistent with the estimates obtained from projecting the information preserved in the upper reaches of the transient river profiles. Results suggest an incision associated with a base level fall in the order of ~1200 m in the Siroua Massif, that decreases gradually to ~500 m in the WAA (Figure 10a). The u^* values in the upstream relict landscape at the maximum elevation are rather uniform with major variations coinciding with the highest mountain peaks composed mostly of quartzites (Figure S6; Clementucci et al., 2022). Finally, the reconstructed paleo-topography indicates a maximum elevation of ~1000 and ~500 m in the central sector of AA and the WAA, respectively before the onset of uplift (Figure 10c). These results are consistent with those obtained from the river projections but with a greater spatial resolution (Figure 10a, 10c). It should be noted that the fitted surface through the relict topography above the incised landscape is less constrained in the Souss and, Draa basins and in the Siroua Massif. In the two basins, aggradation/deposition processes recorded by Plio-Quaternary sedimentary sequences (Hssaine and Bridgland, 2009) are not taken into consideration. Moreover, the maximum elevation obtained for the Siroua Massif represents a maximum estimate because the construction of the volcanic edifice may be coeval or younger than the timing of the fluvial incision, as testified by preserved lava flows along the Siroua escarpment (Figures 6d and 8d).

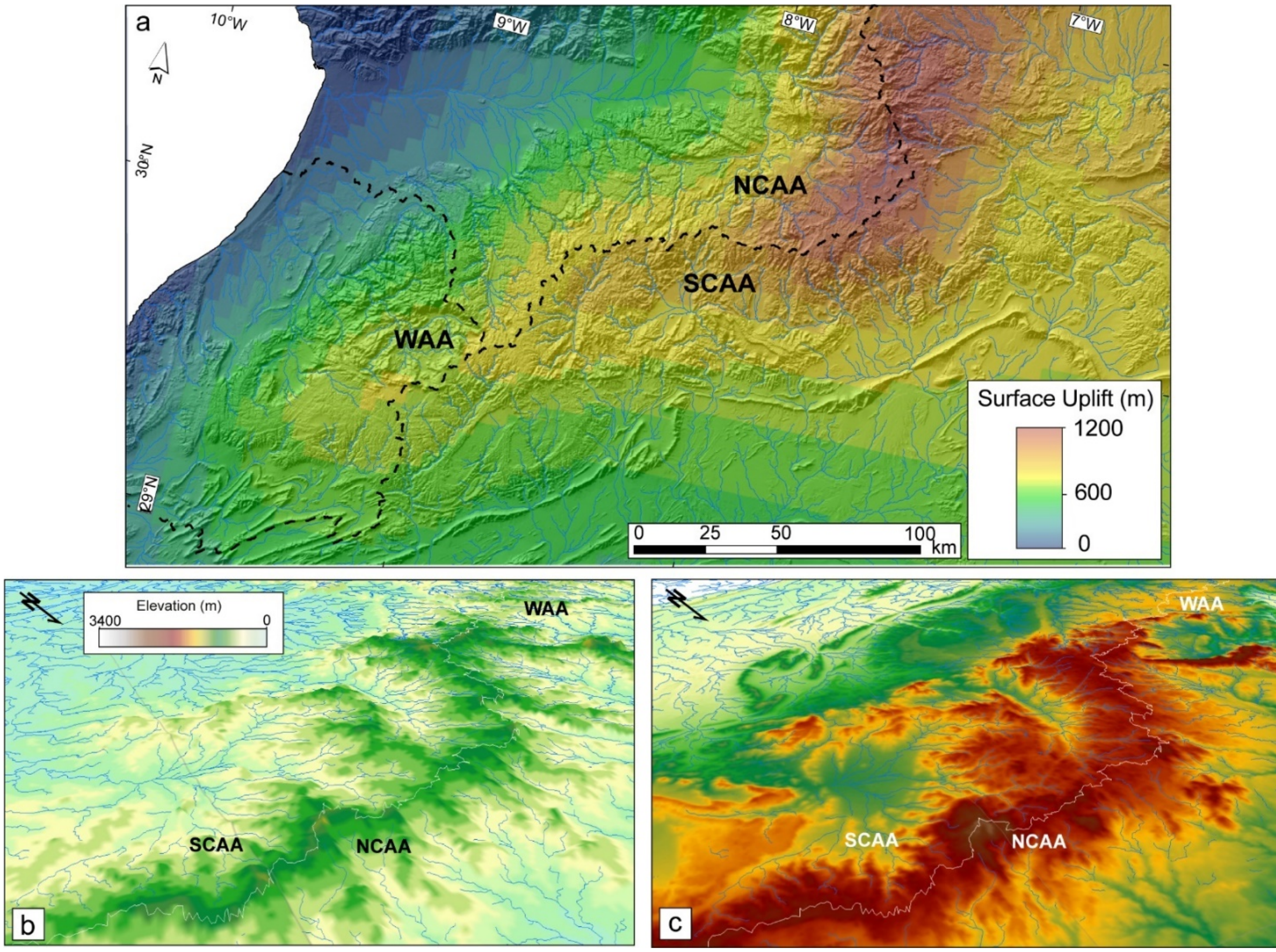

Figure 10. (a) Surface uplift ($S.U.$) map. The base level is defined at the relict landscape boundary; values of $m = 0.45$ and $A_0 = 1$ m^2 were used to calculate and $u*$ (Equation 7). (b) Paleo-topographic reconstruction of the central and western Anti-Atlas. (c) Present-day topography of central and western Anti-Atlas.

1. **Timescales of knickpoint migration**

The time the highest non-lithological knickpoints took to travel from the base level to their present-day position is in the same range of that one required to erode the volume of rocks in a catchment between a high-standing preserved landscape and the minimum topography (*e.g.*, Gallen et al., 2013; Siame et al., 2015). This is called "excavation time" and is generally calculated assuming that erosion took place at constant rates. Denudation rates derived from ^{10}Be concentrations for the Anti-Atlas Mountains are representative mainly for the relict landscape, as discussed in Clementucci et al. (2022). This because the sampled catchments are not representative for the portions of landscape downstream of non-lithological knickpoints, which are mostly composed of carbonate rocks. Hence, denudation rates of 5.8 to 12.5 m/My (Table S4) provide a maximum age for the onset of topographic relief production in the relict landscape of the Anti-Atlas (8.8 to 18.6 Myr in Table S4). Conversely, the highest value of denudation rate (21.3 m/Myr in Table S4) from the Anti-Atlas flank provides a minimum age ~3.8 Myr (Table S4).

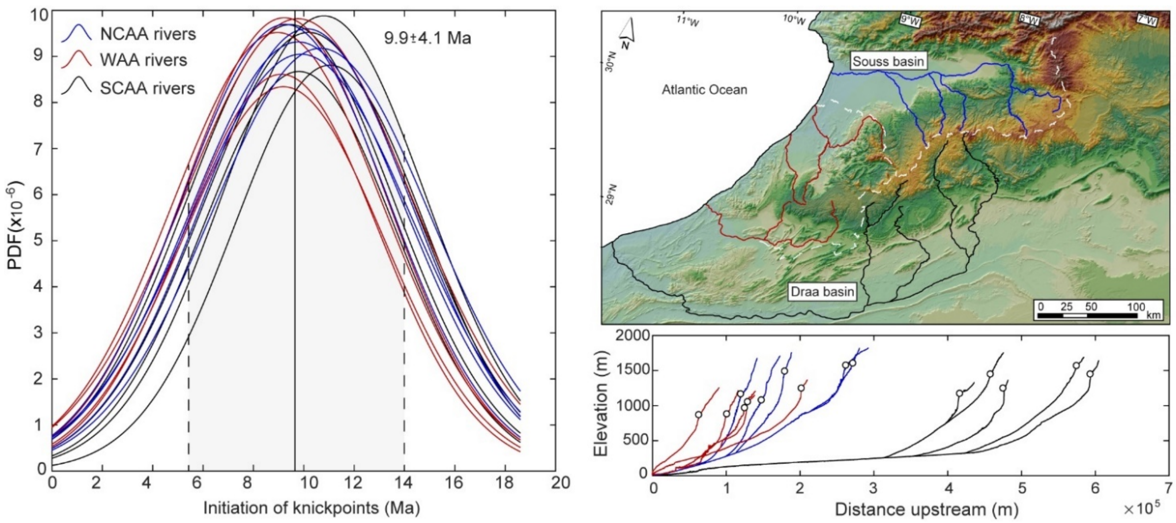

Figure 11. Initiation time of knickpoints propagation in the north, western and southern Anti-Atlas sectors (NCAA, WAA, SCAA). For further information see the table S5 in the supplementary materials.

To constrain the erodibility parameter (K), we used the basin-wide k_{sn} and denudation rates assuming a linear function for the stream power river incision model (n=1). This assumption is justified by the relationships between topographic metrics and normalized channel steepness for tectonically stable regions, as discussed in Clementucci et al. (2022). We considered the present-day river outlets to model the initiation point of the knickpoint propagation. We calculated the basin-averaged k_{sn}, assuming $_{\mathrm{ref}}$ ranging from 0.45 and 0.17 (Figure S5 in the supporting information). These reference values for the Anti-Atlas relict landscape, specifically, most of the values in the relict landscape (upstream knickpoints) are lower than 0.45 (Tables S1 and S2 in the supporting information) and hence we decided to use a reference value of 0.45 to be more conservative. Conversely, 0.17 represents the mean of the concavity estimates for the river sectors of the relict landscape (*i.e.*, upstream the non-lithological knickpoints; Table S1). The results and misfits of modelled knickpoints, using the equation (5), show that the onset of propagation of the base level fall is at 9.9 ± 4.3, 9.2 ± 4.1 and 10.4 ± 4.0 Myr for NCAA, WAA and SCAA sectors, respectively (averaged value 9.9 ± 4.1 Myr; Figure 11 and Table S5). In the Siroua Massif, the volcanic deposits exposed in the plateau are also preserved along the steep valleys in the Siroua escarpment (Figure 6c, 6d, 8d) and consists of ~4-My-old columnar jointed basalts (Berrahma et al., 1995; De Beer et al., 2000). The presence of the volcanic flows at the valley bottom suggests that lavas younger than 4 Myrs, flowed after the valleys formation and knickpoints migration.

1. **Discussion**

5.1 Significance of the transient topography

The strong variation in the normalized channel steepness indices, concavity values, topographic slope, elevation, and fluvial incision between the portions of the landscape downstream and upstream of highest non-lithological knickpoints (Figures 3 and 5) combined with the occurrence of low and uniform erosion rates averaged over different time scales (from late Cretaceous to Quaternary; Clementucci et al., 2022) document a transient condition of the AA topography. This transient state could be attributed to several processes, such as drainage reorganization, climate change, eustatic sea level fall and tectonic uplift (Hancock and Kirwan, 2007; Kirby and Whipple, 2012; Miller et al., 2013, Ballato et al., 2015). Drainage reorganization does not appear to be the cause because of the limited evidence of knickpoints, and wind gaps formation related to river capture processes (Miller et al., 2013). An increase in erosion rates due to climate variations (*i.e.*, increase in precipitation rates) is also unlikely, because such a change would produce a decrease in the channel slopes rather than a steepening (Figure 5; Molnar et al., 2004; Wobus et al., 2010). At the same time a decrease in precipitation rates would produce sediment aggradation, in the lowermost catchment portions and not stepper flanks (Lanari et al., 2022).

Consequently, the abrupt break in the river longitudinal profiles and $-z$ plots at the highest non-lithological knickpoints and the position of the same knickpoints in the space (Figures 5b, 5d, 5f, 8a and S2) indicate that the two portions of the landscape erode at different rates (Schildgen et al., 2012; Miller et al., 2012; 2013; Olivetti et al., 2016). This is consistent with an increase in erosion and rock uplift rates propagating from the river outlet to the uppermost river segments (Miller et al., 2013; Gallen and Wegmann, 2017; Racano et al., 2021). Consequently, the highest knickpoints represent a response of the fluvial system to an increase in rock uplift rates and hence mark a phase of topographic rejuvenation, while the uplifted relict landscape records the previous erosional conditions predating such an increase, as also testified by the spatial distribution of the predicted denudation rates (Figure 12). This implies that the magnitudes of fluvial incision represent minimum estimates of the total amount of surface uplift (*e.g.*, Kirby and Whipple, 2012). A similar scenario has been described in the Appalachian Mountains (Miller et al., 2013) and in other ancient orogens (Olivetti et al., 2012; Scharf et al., 2013; Mandal et al., 2015; Calvet et al., 2015).

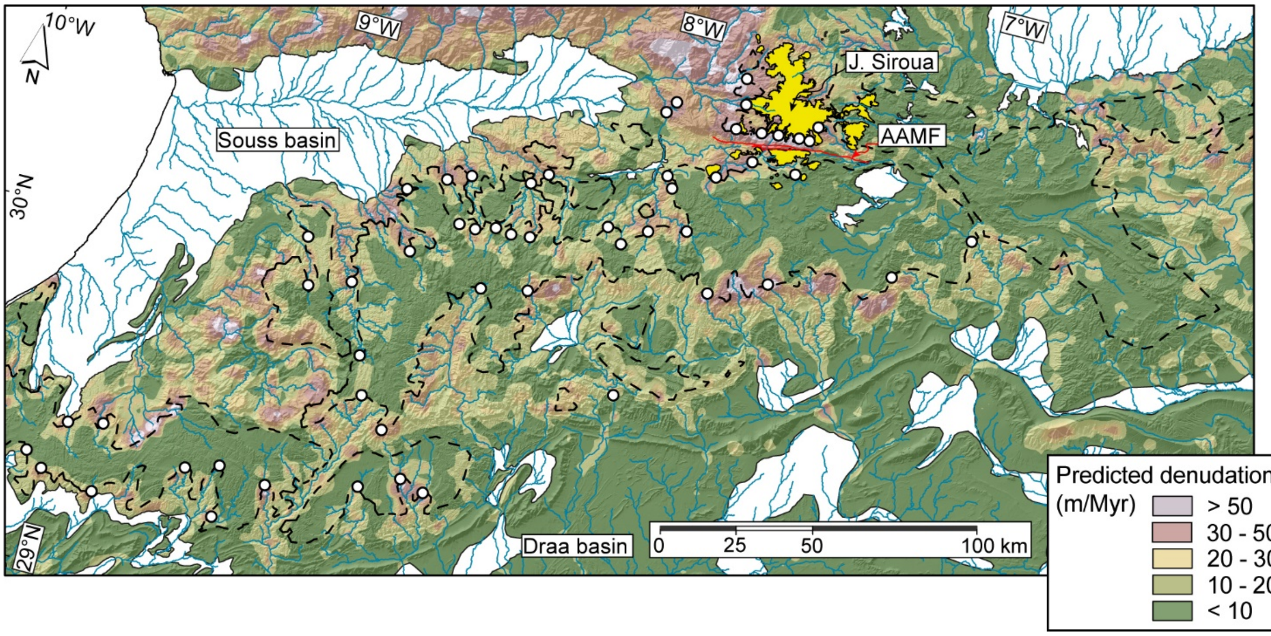

Figure 12. Predicted denudation rates based on the distribution of normalized channel steepness (k_{sn}), using different erodibility values for each lithology (granitic, quartzite basement and sedimentary rocks) and n =1 (after Clementucci et al., 2022).

The minor and non-lithological knickpoints located in the lower segments of the fluvial network, at 700 to 1000 m and from 400 to 500 m in the NCAA, SCAA, and WAA sectors, respectively, can be attributed to a Quaternary climate forcing, eustatic sea-level changes or both (Molnar and England, 1990; Crosby and Whipple, 2006; Hancock and Kirwan, 2007; Ballato et al., 2015). This pattern of knickpoints is spatially consistent and does not show any channel steepness variation across knickpoints in both longitudinal profiles and the $-z$ plot (Figures 5b, 5d, 5f and S2) and hence cannot reflect changes in rock uplift rates.

1. **Topographic evolution of the Anti-Atlas**

A peculiarity of the Anti-Atlas topography is the occurrence of a low-relief topography at its maximum elevation plunging across and along strike over a wavelength of ~ 100 km (Figure 2b, 2c) and ~ 600 km (Figure 2e), respectively, which can be described as a topographic swell. It follows, that the high-standing relict landscape represents a warped geomorphic marker that can be used to document the spatial distribution of the recent increase in surface uplift rates. The along strike pattern of surface uplift ranges from ~500 to 1100 m from the western to the central sector of AA (Figure 9), in agreement with the k_{sn} and elevation pattern of the most elevated non-lithological knickpoints. The paleo-landscape must have been characterized by a low-topographic relief with localized ~1000- to 700-m-high mountain peaks in the central Anti-Atlas (NCAA, SCAA) and the WAA, respectively (Figure 10b and Table S3). These paleo-topographic heights correlate with high normalized channel steepness values observed for low erodibility lithologies, such as quartzite (Figure S6; Clementucci et al., 2022).

The asymmetry of the AA flanks and the different locations of the highest knickpoints between the southern (SCAA) and northern flanks (NCAA) can be attributed to a faster knickpoints migration in the SCAA sector, as also suggested by the occurrence of quasi-equilibrium stream profiles (Figure 5e, 5f). Here, the presence of wide valleys sculptured on synclines within more erodible Paleozoic rocks may have promoted an increase in the contributing drainage area and a faster knickpoint retreat (Figures 4b and S4b, S4c; Crosby and Whippe, 2006; Berlin and Anderson, 2007; Schwanghart and Scherler, 2020). Conversely, in the northern flank, the knickpoint' celerity is lower due to narrower and deeper valleys within less erodible late Precambrian carbonates (Figures 4a and 13c). This highlights the key role that rock strength plays in controlling the valley morphology, and in turn the location of genetically linked knickpoints (*e.g.*, Stokes et al., 2015). Importantly, for the NCAA and SCAA rivers, the migrating wave of transient erosion propagated for several kilometres within the Souss and Draa basins. These regions were likely characterized by erosional processes, before the onset of regional uplift (*e.g.*, Hssaine and Bridgland, 2009). This allows to dismiss a complex scenario with different erodibility parameters within the Neogene-Quaternary sediments in the basins. However, this would not represent an issue because the knickpoint would travel quickly in the mainstream of the Souss and Draa rivers due to the large drainage areas. The knickpoints propagation rate would have decreased one reached the upstream portions of the main mountain front (Crosby and Whipple, 2006; Schwanghart and Scherler, 2020). Hence, the time of residence in the Draa and Souss basins would be negligible. Finally, it should be noted that the occurrence of recent fluvial conglomerates, at high elevation in the major valleys of the northern flank (~700 m) and in the Souss alluvial plain, has been interpreted as an indication that uplift has decreased during the Quaternary (Lanari et al., 2022).

1. **Surface uplift history of Anti-Atlas**

The AA and surrounding basins (e.g., Souss and Ouarzazate) were the southern shoulders of the Triassic-Jurassic rift (Lanari et al., 2020a) as documented by the absence of Mesozoic deposits older than Cretaceous and sediment provenance data (Domènech et al., 2018). During the Cenozoic, the Ouarzazate and Souss basins recorded marine sedimentation at least until the late Eocene, suggesting that part of the study area must have been under sea level until 44 to 42 Ma (Figure 13a; El Harfi et al., 2001; Teson et al., 2010; Hssaine and Bridgland, 2009).

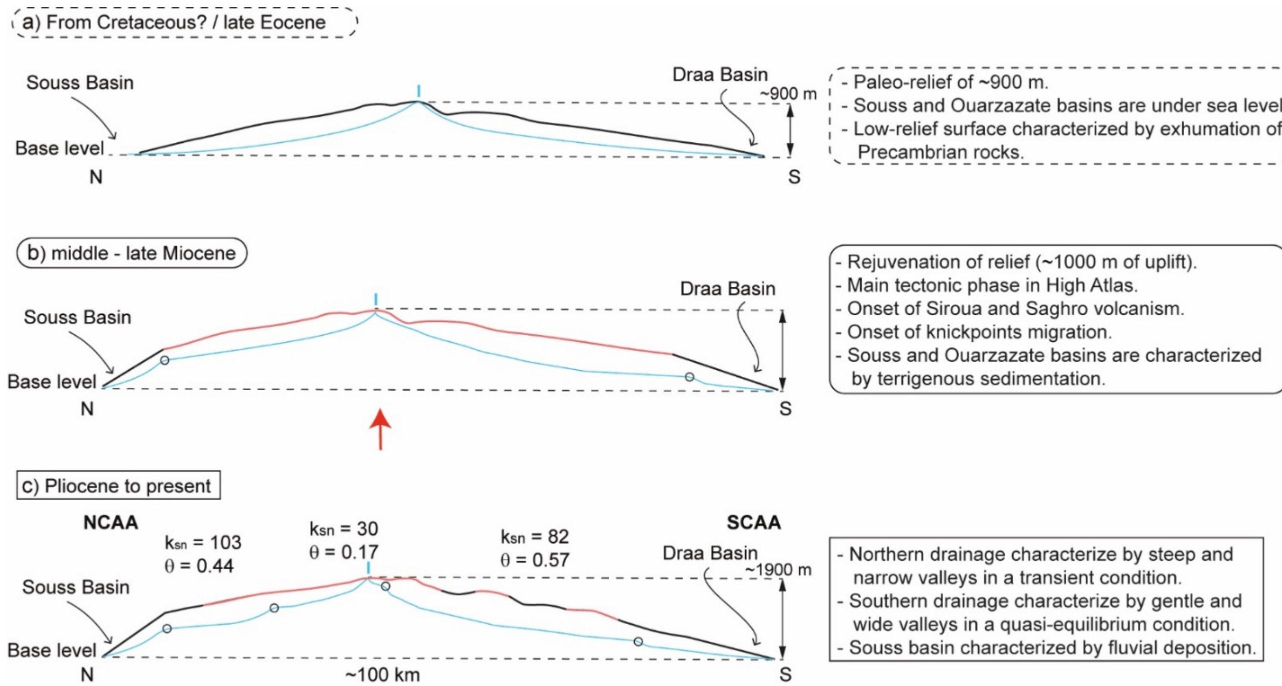

Figure 13. Conceptual model depicting the Anti-Atlas topographic evolution across the central Anti-Atlas. (a) Paleo-topography inferred until the late Eocene. (b) Topographic rejuvenation during the middle-late Miocene associated with the initiation of river incision and knickpoints upstream propagation. (c) Present-day configuration. Pink area describes the preserved relict landscape not yet rejuvenated.

In the AA, the presence of cooling ages older than 70 Ma and consequently the low magnitude of exhumation (< 2-3 km) over the same time interval suggests that the paleo-topography has been developing at least since the late Cretaceous (Figure 13a; Gouiza et al., 2017; Lanari et al., 2020a; Charton et al., 2021; Clementucci et al., 2022). Moreover, our observations and calculations indicate that surface uplift triggered the headward migration of the highest knickpoints starting from the middle-late Miocene (Figures 11 and 13b). These new time constraints suggest average surface uplift rates ranging from 40 to 110 m/Myr (western sector) and from 70 to 180 m/Myr (central sector). These rates are based on the celerity model (9.9 $\pm$ 4.1 Ma) and are averaged over time scales of 14 and 5.8 Ma, using the mean surface uplift values inferred from the river projections (Table S3).

Moreover, predicted denudation rates downstream of non-lithological knickpoints in the adjusted portion of the landscape (Figure 12), show averaged denudation rates up to 50 m/Myr. These rates were obtained multiplying k_{sn} values by bedrock erodibility parameters (K) for different lithologies assuming the stream power model for n = 1 (see details in Clementucci et al., 2022). The predicted denudation rates should reflect uplift rates, assuming a quasi-equilibrium condition of the Anti-Atlas domain (E = U, considering uniform precipitation rates and erodibility values within the same lithologies as discussed in Clementucci et al., 2022). This coincidence suggests that the oldest ages (10 – 14 Ma) estimated from the celerity model may be more representative for the onset of uplift in the Anti-Atlas. This would agree with the onset of volcanic activity in the Siroua Massif where more than 500 km^2 of crystalline basement are covered by 11-to 3-Myr-old lava flows (Figure 13b; Berrahma and Delaoye, 1989; Missenard et al., 2008). Moreover, this age estimates are consistent with the onset of clastic continental sedimentation in the Ouarzazate Basin during the Langhian (16-14 Ma) following an Oligocene to early Miocene sedimentary hiatus (El Harfi et al., 2001; Teson et al., 2010). Finally, the estimated time of topographic rejuvenation in the Anti-Atlas agrees with the onset of contractional deformation in the High Atlas Mountains (Figure 13b; Lanari et al., 2020a).

Instead, the highest range of the uplift rates inferred from the results of our celerity model are more similar to the estimates from the Middle Atlas Mountains (170 – 220 m/Myr, Babault et al., 2008), which are based on uplifted Messinian shallow marine deposits. These observations may indicate that on regional scale, surface uplift was not coeval.

1. **Topographic evolution and surface uplift history of Siroua Massif**

The Siroua Massif is also characterized by a transient topography as documented by the high-standing basement representing the substratum of the Mio-Pliocene volcanic edifice (Figure 8; Missenard et al., 2008). Along the southern margin of the massif, this transient topography is delimited by a pattern of non-lithological knickpoints lying over 2000 m of elevation that on map view are subparallel to the AAMF and cluster along similar values (Figure 8c). The projection of the stream profiles against the AAMF documents about 350 m of surface uplift in the hanging wall of the fault in response to fault activity (Figures 6a, 8c, 8d and 14). Furthermore, short- and long-term denudation rates, estimated from ^{10}Be cosmogenic concentration and eroded volcanic rocks from the Siroua Massif, indicates averaged values of 40-50 m/Myr and 10-20 m/Myr in the adjusted topography downstream and upstream of non-lithological knickpoints, respectively (Figure 12; Clementucci et al., 2022).

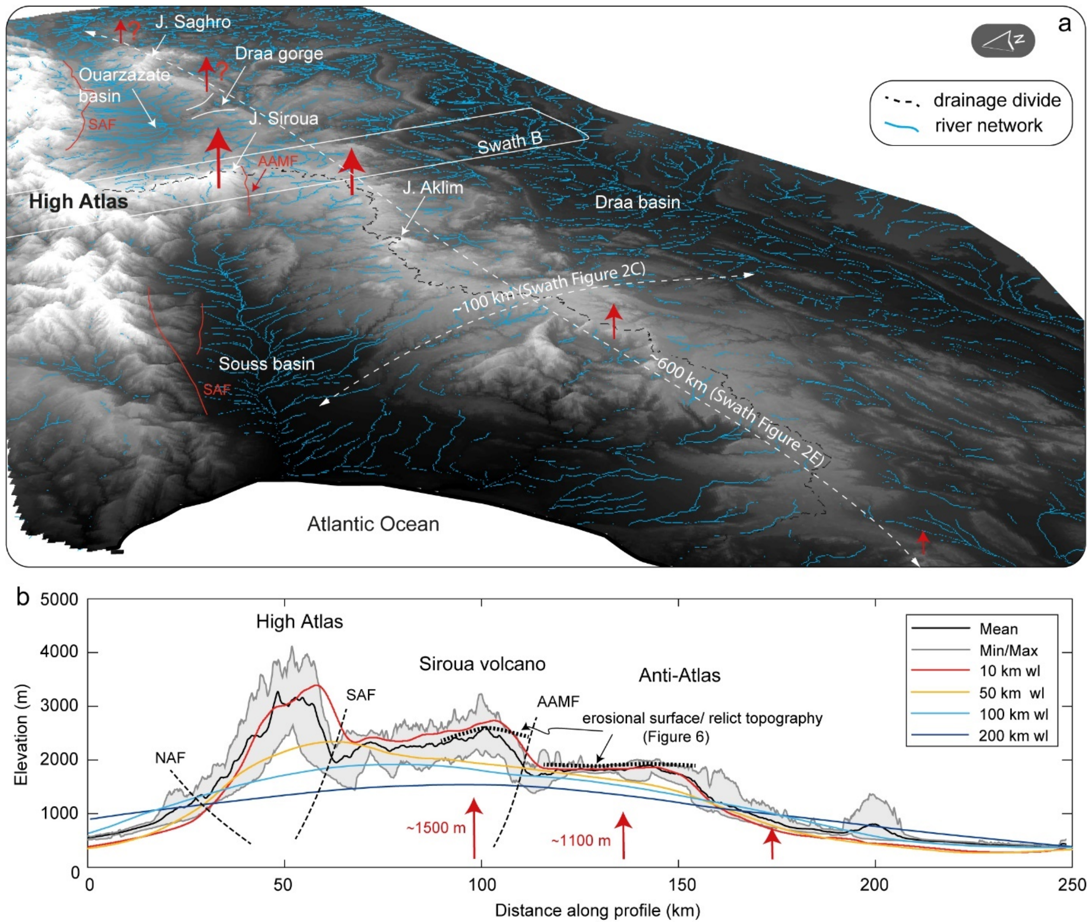

Figure 14. (a) Tridimensional view of the Anti-Atlas region. (b) Swath profile from north to south, showing the local relief and maximum elevation of High Atlas, Siroua Massif and Anti-Atlas. wl: filtered topographic windows. Note that the erosional surface of the Siroua Massif and the Anti-Atlas is standing at more than 2000 m and predated the onset of uplift in the Anti-Atlas and Siroua regions.

This suggest that the summit erosional surface of the AA must be the same surface that one underneath the Siroua volcanic edifice that has been uplifted by the AAMF (Figures 8d and 14b). These conclusions are also consistent with the occurrence of the same volcanic units at different elevations, in the hanging wall and the footwall of the AAMF. Some of these lava flows are also exposed along the steep landscape of the hanging wall of the AAMF downstream of the non-lithological knickpoints. There, they present columnar jointed basalts orthogonal to the valley bottom, suggesting that the valley must have been a reference cooling surface at ~ 4 Ma when the lava was emplaced (Figure 6d).

Consequently, the transient fluvial incision associated with the activity of the AAMF must have started earlier than 4 Ma.

These data allow estimating the contribution of the different mechanisms that produced the modern elevation of ~ 3300 m. Specifically the initial landscape could have been ~ 1000 m of elevation, like the AA (see previous section), while the occurrence of basement rocks beneath the volcano at ~ 2500 m of elevation indicates that volcanic edifice contribute for ~ 800 m high. By subtracting to the modern elevation, 1000 (paleo-topography) and 800 m (volcanic building), we can estimate a surface uplift for the Siroua Massif of ~ 1500 m, where at least 350 meters result from the activity of the AAMF (Figure 14b). A fraction of this ~ 350 m, however, may be associated with the injection of magma at depth as suggested by the dome-like geometry (~ 50 x 100 km) of the basement beneath the Siroua volcano (Missenard et al., 2008). In conclusion, if we exclude the ~ 350 m described above, the regional surface uplift in the Siroua Massif will be ~1150 m in agreement with estimates from the central sectors of the Anti-Atlas.

1. **Causes of surface uplift and topographic expression of the Anti-Atlas and Siroua Massif**

The intracontinental orographic system of the Atlas Mountains represents a natural laboratory for studying the interaction between deep-seated, crustal, and surface processes. The amount of tectonic (crustal) shortening and thickening is limited and in the order of 12 to 35% in the central HA (Beauchamp et al., 1999; Gomez et al., 2000; Teixell et al., 2003; Domènech et al., 2016; Fekkak et al., 2018; Lanari et al., 2020b) and less than 10% in the MA (Gomez et al., 1998; Arboleya et al., 2004). Geophysical evidences, such as heat flow (Rimi et al., 1999; Teixell et al., 2005; Zeyen et al., 2005), gravity anomalies (Ayarza et al., 2005; Missenard et al., 2006), seismological constraints (Seber et al., 1996; Palomeras et al., 2013; Bezada et al., 2013; Miller and Becker, 2014; Spieker et al., 2014) and seismic reflection data (Ayarza et al., 2014) point toward an insufficient thickness of the crust to explain the observed high topography and the anomalously thin lithosphere (~65 km). Geological and geomorphological constraints are consistent with these observations suggesting a contribution of deep-seated processes to the recent regional uplift (Babault et al., 2008; Benabdellouahed et al., 2017; Clementucci et al., 2022). Moreover, the intraplate volcanism of the AA (Siroua and Saghro Massif) and MA is coeval with the main phase of regional uplift inferred in this study for the AA and from thermochronological data in the HA, indicating the occurrence of magmatism during mountain building processes (Berrahma & Delaloye, 1989; El Azzouzi et al., 1999; 2010).

The Atlas system displays short wavelength (10 − 50 km) topographic signals most likely linked to processes operating at crustal scale such as shortening (Teixell et al., 2003; Missenard et al., 2006; Faccenna and Becker, 2020) and long wavelength (> 100 km) signals associated with deeper processes (Figure 14b). Examples of the former and the latter include the HA Mountains and the Meseta, respectively, although multiple processes may concur to produce the observed topography (Teixell et al., 2003; Lanari et al., 2020a). Our study documents that the AA Mountains consists of a topographic swell that has an along- and across-strike wavelength of ~ 600 and 100 km, respectively and a maximum amplitude of ~1100 m (Figures 9b, 10a and 14). This is well underlined by the high-standing surface, which is warped along these two major directions (Figure 14a). The maximum values of surface uplift are observed in the central sector of the AA and appear to be slightly lower than those extracted from the adjacent Siroua Massif where surface uplift results from the sum of a long wavelength, regional uplift, and multiple crustal-scale signals such as faulting along the AAMF and possibly local magma injection. The occurrence of magma intrusions may be testified by the occurrence of a localized topographic bulge on the somital erosional surface of the Siroua that stands beneath the volcano. This would explain the short-wavelength topographic signal observed in figure 14b (Missenard et al., 2008). Similar geomorphic expressions have been described in different settings where magma injection at variable depth in the crust generated a few hundred meters of uplift over different timescales (Singer et al., 2018; Townsend, 2022). This process could have also occurred in the Saghro mountain peak of the eastern Anti-Atlas where a localized maximum topography associated with a few volcanic eruptions is observed (Figure 2e).

The long wavelength topographic swell (600 x 100 km) of the AA, however, still needs to be explained (Figure 14a). Tectonic uplift associated with faulting along a 600-km-long (along strike) crustal scale ramp appears to be unlikely because the AA domain has been tectonically quiescent throughout the entire Cenozoic (Frizon de Lamotte et al., 2009; Lanari et al., 2020a; Clementucci et al., 2022). Furthermore, to explain the ~100-km-long across strike wavelength, one would need a fault-bend-fold mechanisms with a deep flat rooted into the basement, a ramp, and a shallower flat accommodating at least 100 km of displacement. This appears to be quite unlikely, especially if one considers that the AA is a Variscan orogen and not an undisturbed sedimentary multi-layer that may have been detached along stratigraphic horizons. Furthermore, there are no evaporite layers in the pre Variscan sedimentary sequence that could accommodate such an amount of displacement, as observed in the adjacent HA (Lanari et al., 2020b). These observations suggest that the ~ 600 x 100 km AA topographic swell could be only explained through a deeper processes (mantle activity).

A major deep-seated mechanism, which has been invoked as main contributor in the construction of elevated orogenic plateaus is the delamination of the lithospheric mantle and possibly of the lower crust (*e.g.*, Garzione et al., 2006; Hatzfeld and Molnar, 2010). This would change the density structure of lithosphere through the sinking of a relatively dense lithospheric mantle and the rise of a hotter and less dense asthenosphere. This hypothesis requires the occurrence of a previously thickened lithosphere, which does not appear to be the case for the AA where crustal shortening and thickening processes following the Variscan orogeny have been very limited (Burkhard et al., 2006). Moreover, the occurrence of a thickened lithosphere would have produced a large-scale subsidence with associated subsidence and sedimentation before the onset of uplift, and this is not supported by stratigraphic data, which suggest subaerial erosional conditions at least since the late Cretaceous (Gouiza et al., 2017; Clementucci et al., 2022). In intracontinental areas, another possible mechanism is the upwelling of asthenospheric mantle (Duggen et al., 2009; Faccenna et al., 2013; Miller et al., 2013; Olivetti et al., 2016; Faccenna and Becker, 2020). Independently from the geodynamic setting and the main reasons for such a rise, the upward movement of hot asthenospheric mantle generates a deflection of the lithosphere in association with adiabatic melting and production of a magma with an alkaline signature (*e.g.*,Wilson and Downes, 1991; Gibson et al., 2006). This process will generate a strong positive free air anomaly (Faccenna and Becker, 2020). This appears to be the case for the AA, where all observations are met (Berrahma and Delaloye, 1989; Spieker et al., 2014). Moreover, the wavelength recorded in the topography of the AA is compatible with other examples from the oceanic floor, where larger-scale swell signals have been observed (Cserepes et al., 2000). Tomography analysis also suggests mantle upwelling in NW Africa, which may be associated with plume activity recorded in the Atlantic Ocean in the Canary Islands (Duggen et al., 2009; Civiero et al., 2019). In conclusion, our topographic analysis indicates that the topography of the Anti-Atlas appears to be consistent with asthenospheric upwelling processes although the cause of these deep-seated mechanism and the possible genetic link with the Canary Islands remain still poorly understood.

Conclusion

Our study allows characterizing modern and past topography of the Anti-Atlas Mountains and inferring its surface uplift history. In particular, we show that:

1) The landscape is in a transient state and exhibits a main pattern of elevated non-lithological knickpoints that mark a regional transition, from high to low values of topographic and channel metrics. The topography upstream of the non-lithological knickpoints can be described as an erosional surface (relict landscape) that plunges along and across strike. Our paleo-topographic reconstruction suggests that such an erosional surface formed a subdued topography with a few local peaks in the order of ~ 1000 m of elevation that started to develop from the late Cretaceous.

2) The magnitude of surface uplift increases along-strike from the western Anti-Atlas (500 m) to the central Anti-Atlas (1100 m) and the Siroua Massif (1500 m), where the latter represents a main Mio-Pliocene regional volcanic centre. Geometrically, the surface uplift can be described as ~ 600 x 100 km swell. The initiation of knickpoints migration marks the onset of topographic rejuvenation and is estimated to be middle-late Miocene (9.9 ± 4.1 Ma). This is coeval with the initiation of a main tectonic phase in the High Atlas and with volcanism in the Siroua and the Saghro Massifs. Surface uplift occurred at rates of 40 to 110 m/Myr and 70 to 180 m/My, (averaged over time scales of 14 and 5.8 Ma) that gradually increase from the western to the central Anti-Atlas, respectively. Our higher rate estimates fall within the same range of values inferred from Messinian shallow marine deposits of the Middle Atlas.

3) Surface uplift in the Siroua Massif is higher than in the Anti-Atlas because it results from the contribution of different signals, such as the long-wavelength regional component (i.e., the topographic swell; ~ 1150 m), the growth of a volcanic edifice (~ 800 m), faulting along the Anti-Atlas Major Fault (~ 350 m) and possibly magma injection processes which cannot be easily quantified but may be included in the contribution ascribed to faulting.

4) The long wavelength (~ 600 x 100 km) topographic swell documented through the topographic analysis can be explained by upwelling of hot asthenosphere (mantle process).Mantle upwelling is also responsible for the generation of magmatism in the Siroua and Saghro Massif. Although the genesis of such a rise is unknown, it appears to be the only feasible mechanisms.

In conclusion, our data provide new constrains for deciphering the complex history of topographic growth resulting from the interplay between shallower and deep-seated processes.

Acknowledgments

This study is part of the PhD thesis of RC at the University of Roma Tre (PhD Cycle XXXIV). It was supported by the PhD School of Roma Tre and grant "Vinci 2020" awarded to RC (Number: C2-1403). PB was supported by the MIUR (Ministry of Education University and Research), Excellence Department Initiative, Art. 1, com. 314-337, Low 232/2016. The ASTER (CEREGE, Aix-en-Provence) AMS national facility, is supported by the INSU/CNRS, and the IRD. We thank P-H Blard, S. Willett and T. Schildgen for revising this manuscript as a chapter of the PhD Thesis of the RC, to L. Benedetti, M. Della Seta, P. Molin and O. Bellier for providing valuable comments during the PhD defense of RC. The Supporting Information is available online (https://osf.io/fnvke/).

References

Ait Malek, H. A., Gasquet, D., Bertrand, J. M., & Leterrier, J. (1998). Géochronologie U-Pb sur zircon de granitoïdes éburnéens et panafricains dans les boutonnières protérozoïques d'Igherm, du Kerdous et du Bas Drâa (Anti-Atlas occidental, Maroc). *Comptes Rendus de l'Académie des Sciences-Series IIA-Earth and Planetary Science*, *327*(12), 819-826. https://doi.org/10.1016/S1251-8050(99)80056-1

Arboleya, M. L., Teixell, A., Charroud, M., & Julivert, M. (2004). A structural transect through the High and Middle Atlas of Morocco. *Journal of African Earth Sciences*, 39(3–5), 319–327. https://doi.org/10.1016/j.jafrearsci.2004.07.036

Arboleya, M.-L., Babault, J., Owen, L. A., Teixell, A., & Finkel, R. C. (2008). Timing and nature of Quaternary fluvial incision in the Ouarzazate foreland basin, Morocco. *Journal of the Geological Society*, 165(6), 1059–1073. https://doi.org/10.1144/0016-76492007-151

Ayarza, P., Alvarez-Lobato, F., Teixell, A., Arboleya, M. L., Teson, E., Julivert, M., & Charroud, M. (2005). Crustal structure under the central High Atlas Mountains (Morocco) from geological and gravity data. *Tectonophysics*, *400*(1-4), 67-84. https://doi.org/10.1016/j.tecto.2005.02.009

Azizi Samir, M. R., Ferrandini, J., & Tane, J. L. (1990). Tectonique et volcanisme tardi-Pan Africains (580-560 Ma) dans l'Anti-Atlas Central (Maroc): interprétation géodynamique à l'échelle du NW de l'Afrique. *Journal of African Earth Sciences*, *10*(3), 549-563. https://doi.org/10.1016/0899-5362(90)90105-N

Babault, J., Teixell, A., Arboleya, M. L., & Charroud, M. (2008). A Late Cenozoic age for long-wavelength surface uplift of the Atlas Mountains of Morocco. *Terra nova*, *20*(2), 102-107. https://doi.org/10.1111/j.1365-3121.2008.00794.x

Baldwin, J. A., Whipple, K. X., & Tucker, G. E. (2003). Implications of the shear stress river incision model for the timescale of postorogenic decay of topography. *Journal of Geophysical Research: Solid Earth*, 108(B3). https://doi.org/10.1029/2001JB000550.

Balestrieri, M. L., Moratti, G., Bigazzi, G., & Algouti, A. (2009). Neogene exhumation of the Marrakech High Atlas (Morocco) recorded by apatite fission-track analysis. Terra Nova, 21(2), 75–82. https://doi.org/10.1111/j.1365-3121.2008.00857.x

Ballato, P., Landgraf, A., Schildgen, T. F., Stockli, D. F., Fox, M., Ghassemi, M. R., Kirby, E., & Strecker, M. R. (2015). The growth of a mountain belt forced by base-level fall: Tectonics and surface processes during the evolution of the Alborz Mountains, N Iran. *Earth and Planetary Science Letters*, *425*, 204-218. https://doi.org/10.1016/j.epsl.2015.05.051

Barbero, L., Teixell, A., Arboleya, M. L., del Río, P., Reiners, P. W., & Bougadir, B. (2007). Jurassic-to-present thermal history of the central High Atlas (Morocco) assessed by low-temperature thermochronology. *Terra Nova*, 19(1), 58–64. https://doi.org/10.1111/j.1365-3121.2006.00715.x

Baudon, C., Fabuel-Perez, I., & Redfern, J. (2009). Structural style and evolution of a Late Triassic rift basin in the central High Atlas, Morocco: Controls on sediment deposition. *Geological Journal*, 44(6), 677–691. https://doi.org/10.1002/gj.1195

Beauchamp, W., Allmendinger, R. W., Barazangi, M., Demnati, A., El Alji, M., & Dahmani, M. (1999). Inversion tectonics and the evolution of the High Atlas Mountains, Morocco, based on a geological-geophysical transect. *Tectonics,* 18(2), 163–184. https://doi.org/10.1029/1998TC900015

Benabdellouahed, M., Klingelhoefer, F., Gutscher, M. A., Rabineau, M., Biari, Y., Hafid, M., Duarte J. C., Schnabel M., Baltzer A., Pedoja K., Le Roy P., Reichert C., & Sahabi, M. (2017). Recent uplift of the Atlantic Atlas (offshore

West Morocco): Tectonic arch and submarine terraces. *Tectonophysics*, *706*, 46-58. https://doi.org/10.1016/j.tecto.2017.03.024

Berlin, M. M., & Anderson, R. S. (2007). Modeling of knickpoint retreat on the Roan Plateau, western Colorado. *Journal of Geophysical Research: Earth Surface*, *112*(F3). https://doi.org/10.1029/2006JF000553

Berrahma, M., & Delaloye, M. (1989). Données géochronologiques nouvelles sur le massif volcanique du Siroua (Anti-Atlas, Maroc). *Journal of African Earth Sciences (and the Middle East)*, 9(3-4), 651-656.https://doi.org/10.1016/0899-5362(89)90049-3.

Berrahma, M. (1995). Etudes pétrologiques des laves récentes du massif du Siroua (Anti-Atlas, Maroc). Éd. du Service Géologique du Maroc.

Bezada, M. J., Humphreys, E. D., Davila, J. M., Carbonell, R., Harnafi, M., Palomeras, I., & Levander, A. (2014). Piecewise delamination of Moroccan lithosphere from beneath the Atlas Mountains. *Geochemistry, Geophysics, Geosystems*, *15*(4), 975-985. https://doi.org/10.1002/2013GC005059

Burkhard, M., Caritg, S., Helg, U., Robert-Charrue, C., & Soulaimani, A. (2006). Tectonics of the anti-Atlas of Morocco. *Comptes Rendus Geoscience*, *338*(1-2), 11-24. https://doi.org/10.1016/j.crte.2005.11.012.

Calvet, M., Gunnell, Y., & Farines, B. (2015). Flat-topped mountain ranges: Their global distribution and value for understanding the evolution of mountain topography. *Geomorphology*, *241*, 255-291. https://doi.org/10.1016/j.geomorph.2015.04.015

Charton, R., Bertotti, G., Arnould, A. D., Storms, J. E., & Redfern, J. (2021). Low-temperature thermochronology as a control on vertical movements for semi-quantitative source-to-sink analysis: A case study for the Permian to Neogene of Morocco and surroundings. *Basin Research*, *33*(2), 1337-1383. https://doi.org/10.1111/bre.12517

Choubert, G. (1952). Histoire géologique du domaine de l'Anti-Atlas. *Notes et Mém. Serv. Géol. Maroc*, (100), 77-172.

Civiero, C., Custódio, S., Rawlinson, N., Strak, V., Silveira, G., Arroucau, P., & Corela, C. (2019). Thermal nature of mantle upwellings below the Ibero-western Maghreb region inferred from teleseismic tomography. *Journal of Geophysical Research: Solid Earth*, *124*(2), 1781-1801. https://doi.org/10.1029/2018JB016531

Clementucci, R. (2022). Deciphering mantle contribution on surface uplift in the Atlas-Meseta system (Morocco) (Doctoral dissertation). Earth Sciences. Università degli studi Roma Tre; Aix Marseille Univ. https://tel.archives-ouvertes.fr/tel-03630297/document

Crosby, B. T., & Whipple, K. X. (2006). Knickpoint initiation and distribution within fluvial networks: 236 waterfalls in the Waipaoa River, North Island, New

Zealand. *Geomorphology*, *82*(1-2), 16-38. https://doi.org/10.1016/j.geomorph.2005.08.023

Cserepes, L., Christensen, U. R., & Ribe, N. M. (2000). Geoid height versus topography for a plume model of the Hawaiian swell. *Earth and Planetary Science Letters*, *178*(1-2), 29-38. https://doi.org/10.1016/S0012-821X(00)00065-0

De Beer, C. H., Chevallier, L. P., De Kock, G. S., Gresse, P. G., & Thomas, R. J. (2000). Mémoire explicatif de la carte géologique du Maroc au 1/50 000, Feuille Sirwa. *Notes Mem. Serv. Geol. Maroc*, *395*, 86.

DeCelles, P. G., Ducea, M. N., Kapp, P., & Zandt, G. (2009). Cyclicity in Cordilleran orogenic systems. *Nature Geoscience*, *2*(4), 251-257. https://doi.org/10.1038/ngeo469

DiBiase, R. A., & Whipple, K. X. (2011). The influence of erosion thresholds and runoff variability on the relationships among topography, climate, and erosion rate. *Journal of Geophysical Research: Earth Surface*, *116*(F4). http://dx.doi.org/10.1029/2011JF002095.

Domènech, M., Teixell, A., Babault, J., & Arboleya, M. L. (2015). The inverted Triassic rift of the Marrakech High Atlas: A reappraisal of basin geometries and faulting histories. *Tectonophysics,* 663, 177–191. https://doi.org/10.1016/j.tecto.2015.03.017

Domènech, M., Teixell, A., & Stockli, D. F. (2016). Magnitude of rift-related burial and orogenic contraction in the Marrakech High Atlas revealed by zircon (U-Th)/He thermochronology and thermal modeling. *Tectonics*, 35(11), 2609–2635. https://doi.org/10.1002/2016TC004283

Domènech, M., Stockli, D. F., & Teixell, A. (2018). Detrital zircon U–Pb provenance and palaeogeography of Triassic rift basins in the Marrakech High Atlas. *Terra Nova*, 30(4), 310-318. https://doi.org/10.1111/ter.12340

Duggen, S., Hoernle, K. A., Hauff, F., Kluegel, A., Bouabdellah, M., & Thirlwall, M. F. (2009). Flow of Canary mantle plume material through a subcontinental lithospheric corridor beneath Africa to the Mediterranean. *Geology*, *37*(3), 283-286. https://doi.org/10.1130/G25426A.1

Duvall, A., Kirby, E., & Burbank, D. (2004). Tectonic and lithologic controls on bedrock channel profiles and processes in coastal California. *Journal of Geophysical Research: Earth Surface*, 109(F3). https://doi.org/10.1029/2003JF000086

El Azzouzi, M., Bellon, H., Maury, R. C., Pique, A., Cotten, J., Griffiths, J. B., ... & Hernandez, J. (1999). Evolution of the sources of Moroccan volcanism during the Neogene. *Comptes Rendus de l'Academie des Sciences. Serie 2, Sciences de la Terre et des Planetes*, 95-102.

El Azzouzi, M. H., Maury, R. C., Bellon, H., Youbi, N., Cotten, J., & Kharbouch, F. (2010). Petrology and K-Ar chronology of the Neogene-quaternary

Middle Atlas basaltic province, Morocco. *Bulletin de la société géologique de France*, *181*(3), 243-257. https://doi.org/10.2113/gssgfbull.181.3.243

El Harfi, A., Lang, J., Salomon, J., & Chellai, E. H. (2001). Cenozoic sedimentary dynamics of the ouarzazate foreland basin (Central High Atlas Mountains, Morocco). *International Journal of Earth Sciences*, 90, 393–411. https://doi.org/10.1007/s005310000115

England, P., & Molnar, P. (1990). Surface uplift, uplift of rocks, and exhumation of rocks. *Geology*, *18*(12), 1173-1177. https://doi.org/10.1130/0091-7613(1990)018%3c1173:SUUORA%3e2.3.CO;2

Faccenna, C., Becker, T. W., Conrad, C. P., & Husson, L. (2013). Mountain building and mantle dynamics. *Tectonics*, *32*(1), 80-93. https://doi.org/10.1029/2012TC003176

Faccenna, C., & Becker, T. W. (2020). Topographic expressions of mantle dynamics in the Mediterranean. *Earth-Science Reviews*, 103327. https://doi.org/10.1016/j.earscirev.2020.103327

Fekkak, A., Ouanaimi, H., Michard, A., Soulaimani, A., Ettachfini, E. M., Berrada, I., et al. (2018). Thick-skinned tectonics in a Late Cretaceous-Neogene intracontinental belt (High Atlas Mountains, Morocco): The flat-ramp fault control on basement shortening and cover folding. Journal of African Earth Sciences, 140, 169–188. https://doi.org/10.1016/j.jafrearsci.2018.01.008

Flint, J. J. (1974). Stream gradient as a function of order, magnitude, and discharge. *Water Resources Research*, 10, 969–973.

Forte, A. M., & Whipple, K. X. (2019). Short communication: The Topographic Analysis Kit (TAK) for TopoToolbox, *Earth Surface Dynamics*. 7, 87–95. https://doi.org/10.5194/esurf-7-87-2019.

Fox, M. (2019). A linear inverse method to reconstruct paleo-topography. *Geomorphology*, *337*, 151-164. https://doi.org/10.1016/j.geomorph.2019.03.034

Fox, M., & Carter, A. (2020). How continuous are the "Relict" landscapes of Southeastern Tibet?. *Frontiers in Earth Science*, *8*(587597). https://doi.org/10.3389/feart.2020.587597

Fraissinet, C., El Zouine, M., Morel, J. L., Poisson, A., Andrieux, J., & Faure-Muret, A. (1988). Structural evolution of the southern and northern central High Atlas in Paleogene and Mio-Pliocene times. In *The Atlas System of Morocco* (pp. 273-291). Springer, Berlin, Heidelberg.

Frizon de Lamotte, D., Saint Bezar, B., Bracène, R., & Mercier, E. (2000). The two main steps of the Atlas building and geodynamics of the western Mediterranean. *Tectonics*, 19, 740–761. https://doi.org/10.1029/2000TC900003

Frizon de Lamotte, D., Leturmy, P., Missenard, Y., Khomsi, S., Ruiz, G., Saddiqi, O., Guillocheau F., & Michard A. (2009). Mesozoic and Cenozoic vertical movements in the Atlas system (Algeria, Morocco, Tunisia). An overview: *Tectonophysics*. 475, 9–28. https://doi.org/10.1016/j.tecto.2008.10.024.

Froitzheim, N., Stets, J., & Wurster, P. (1988). Aspects of western High Atlas tectonics. *In The Atlas System of Morocco*, (pp. 219–244). Berlin: Springer.

Gallen, S. F., Wegmann, K. W., & Bohnenstiehl, D. R. (2013). Miocene rejuvenation of topographic relief in the southern Appalachians. *GSA Today*, *23*(2), 4-10. https://doi.org/10.1130/GSATG163A.1.

Gallen, S. F., & Wegmann, K. W. (2017). River profile response to normal fault growth and linkage: An example from the Hellenic forearc of south-central Crete, Greece. *Earth Surface Dynamics*, *5*(1), 161-186. https://doi.org/10.5194/esurf-5-161-2017

Gallen, S. F. (2018). Lithologic controls on landscape dynamics and aquatic species evolution in post-orogenic mountains. *Earth and Planetary Science Letters*, *493*, 150-160. https://doi.org/10.1016/j.epsl.2018.04.029.

Garzione, C. N., Molnar, P., Libarkin, J. C., & MacFadden, B. J. (2006). Rapid late Miocene rise of the Bolivian Altiplano: Evidence for removal of mantle lithosphere. *Earth and Planetary Science Letters*, *241*(3-4), 543-556. https://doi.org/10.1016/j.epsl.2005.11.026

Gasquet, D., Ennih, N., Liégeois, J. P., Soulaimani, A., & Michard, A. (2008). The pan-african belt. In *Continental evolution: the geology of Morocco* (pp. 33-64). Springer, Berlin, Heidelberg. https://doi.org/10.1007/978-3-540-77076-3_2

Ghorbal, B., Bertotti, G., Foeken, J., & Andriessen, P. (2008). Unexpected Jurassic to Neogene vertical movements in 'stable'parts of NW Africa revealed by low temperature geochronology. *Terra Nova*, *20*(5), 355-363. https://doi.org/10.1111/j.1365-3121.2008.00828.x

Gibson, S. A., Thompson, R. N., & Day, J. A. (2006). Timescales and mechanisms of plume–lithosphere interactions: 40Ar/39Ar geochronology and geochemistry of alkaline igneous rocks from the Paraná–Etendeka large igneous province. *Earth and Planetary Science Letters*, *251*(1-2), 1-17. https://doi.org/10.1016/j.epsl.2006.08.004

Gomez, F., Allmendinger, R., Barazangi, M., Er-Raji, A., & Dahmani, M. (1998). Crustal shortening and vertical strain partitioning in the Middle Atlas Mountains of Morocco. *Tectonics*, *17*(4), 520-533. https://doi.org/10.1029/98TC01439

Gomez, F., Beauchamp, W., & Barazangi, M. (2000). Role of the Atlas Mountains (northwest Africa) within the African-Eurasian plate-boundary zone. *Geology*, 28(9), 775–778. https://doi.org/10.1130/0091-7613(2000)28%3c775:ROTAMN%3e2.0.CO;2

Görler, K., Helmdach, F.-F., Gaemers, P., Heißig, K., Hinsch, W., Mädler, K., et al. (1988). The uplift of the central High Atlas as deduced from Neogene continental sediments of the Ouarzazate province, Morocco. In *The Atlas System of Morocco*, (pp. 359–404). Berlin: Springer. https://doi.org/10.1007/s00531-016-1325-0

Gouiza, M., Charton, R., Bertotti, G., Andriessen, P., & Storms, J. E. A. (2017). Post-Variscan evolution of the Anti-Atlas belt of Morocco constrained from low-temperature geochronology. *International Journal of Earth Sciences*, *106*(2), 593-616.

Guimerà, J., Arboleya, M. L., & Teixell, A. (2011). Structural control on present-day topography of a basement massif: the Central and Eastern Anti-Atlas (Morocco). *Geologica Acta: an international earth science journal*, *9*(1), 55-65. https://doi.org/10.1344/105.00 0001643.

Hack, J. T. (1957). *Studies of longitudinal stream profiles in Virginia and Maryland* (Vol. 294). US Government Printing Office.

Hafid, M. (2000). Triassic-early Liassic extensional systems and their Tertiary inversion, Essaouira Basin (Morocco). *Marine and Petroleum Geology*, 17, 409–429. https://doi.org/10.1016/S0264-8172(98)00081-6

Hancock, G., & Kirwan, M. (2007). Summit erosion rates deduced from 10Be: Implications for relief production in the central Appalachians. *Geology*, *35*(1), 89-92. https://doi.org/10.1130/G23147A.1

Harkins, N., Kirby, E., Heimsath, A., Robinson, R., & Reiser, U. (2007). Transient fluvial incision in the headwaters of the Yellow River, northeastern Tibet, China. *Journal of Geophysical Research: Earth Surface*, *112*(F3). https://doi.org/10.1029/2006JF000570

Hatzfeld, D., & Molnar, P. (2010). Comparisons of the kinematics and deep structures of the Zagros and Himalaya and of the Iranian and Tibetan plateaus and geodynamic implications. *Reviews of Geophysics*, *48*(2). https://doi.org/10.1029/2009RG000304

Hefferan, K. P., Admou, H., Karson, J. A., & Saquaque, A. (2000). Anti-atlas (Morocco) role in neoproterozoic western Gondwana reconstruction. *Precambrian Research*, 103(1-2), 89-96. https://doi.org/10.1016/S0301-9268(00)00078-4

Heidarzadeh, G., Ballato, P., Hassanzadeh, J., Ghassemi, M. R., & Strecker, M. R. (2017). Lake overspill and onset of fluvial incision in the Iranian Plateau: Insights from the Mianeh Basin. *Earth and Planetary Science Letters*, 469, 135-147. https://doi.org/10.1016/j.epsl.2017.04.019

Helg, U., Burkhard, M., Caritg, S., & Robert-Charrue, C. (2004). Folding and inversion tectonics in the anti-Atlas of Morocco. *Tectonics*, *23*(4). https://doi.org/10.1029/2003TC001576

Hollard, H., Choubert, G., Bronner, G., Marchand, J., Sougy, J. (1985). Carte géologique du Maroc, scale 1: 1,000,000. *Serv. Carte géol. Maroc.* 260(2).

Howard, A. D., & Kerby, G. (1983). Channel changes in badlands. *Geological Society of America Bulletin*, *94*(6), 739-752. http://dx.doi.org/10.1130/0016-7606(1983)94%3c739:CCIB%3e2.0.CO;2.

Howard, A. D. (1994). A detachment-limited model of drainage basin evolution. *Water resources research*, *30*(7), 2261-2285. https://doi.org/10.1029/94WR00757

Hssaine, A. A., & Bridgland, D. (2009). Pliocene–Quaternary fluvial and aeolian records in the Souss Basin, southwest Morocco: A geomorphological model. *Global and Planetary Change*, 68, 288–296. https://doi.org/10.1016/j.gloplacha.2009.03.002

Jansen, J. D., Codilean, A. T., Bishop, P., & Hoey, T. B. (2010). Scale dependence of lithological control on topography: Bedrock channel geometry and catchment morphometry in western Scotland. *The Journal of geology*, *118*(3), 223-246. https://doi.org/10.1086/651273.

Kirby, E., & Whipple, K. (2001). Quantifying differential rock-uplift rates via stream profile analysis. *Geology*, *29*(5), 415-418. https://doi.org/10.1130/0091-7613(2001)029%3c0415:QDRURV%3e2.0.CO;2.

Kirby, E., & Whipple, K. X. (2012). Expression of active tectonics in erosional landscapes. *Journal of Structural Geology*, *44*, 54-75. https://doi.org/10.1016/j.jsg.2012.07.009.

Lanari, R., Fellin, M. G., Faccenna, C., Balestrieri, M. L., Pazzaglia, F. J., Youbi, N., & Maden, C. (2020a). Exhumation and surface evolution of the western high atlas and surrounding regions as constrained by low-temperature thermochronology. *Tectonics*, *39*(3), e2019TC005562. https://doi.org/10.1029/2019TC005562

Lanari, R., Faccenna, C., Fellin, M. G., Essaifi, A., Nahid, A., Medina, F., & Youbi, N. (2020b). Tectonic evolution of the western high Atlas of Morocco: oblique convergence, reactivation, and transpression. *Tectonics*, *39*(3), e2019TC005563. https://doi.org/10.1029/2019TC005563

Lanari, R., Reitano, R., Giachetta, E., Pazzaglia, F. J., Clementucci, R., Faccenna, C., & Fellin, M. G. (2022). Is the Anti-Atlas of Morocco still uplifting?. *J. Afr. Earth. Sci.*, 188, 104481. https://doi.org/10.1016/j.jafrearsci.2022.104481

Leblanc, M. (1975). Ophiolites précambriennes et gites arseniés de cobalt: Bou Azzer (Maroc). *These Doctorat d'Etat, Faculte des Science Paris VI, Memoires Centre Geologique et Geophysique.*

Leprêtre, R., Missenard, Y., Barbarand, J., Gautheron, C., Jouvie, I., & Saddiqi, O. (2018). Polyphased inversions of an intracontinental rift: Case study of the

Marrakech High Atlas, Morocco. *Tectonics*, 37(3), 818–841. https://doi.org/10.1002/2017TC004693

Malusa, M. G., Polino, R., Feroni, A. C., Ellero, A., Ottria, G., Baidder, L., & Musumeci, G. (2007). Post-Variscan tectonics in eastern anti-atlas (Morocco). *Terra Nova*, *19*(6), 481-489. https://doi.org/10.1111/j.1365-3121.2007.00775.x

Mandal, S. K., Lupker, M., Burg, J. P., Valla, P. G., Haghipour, N., & Christl, M. (2015). Spatial variability of 10Be-derived erosion rates across the southern Peninsular Indian escarpment: A key to landscape evolution across passive margins. *Earth and Planetary Science Letters*, *425*, 154-167. https://doi.org/10.1016/j.epsl.2015.05.050.

Miller, S. R., Baldwin, S. L., & Fitzgerald, P. G. (2012). Transient fluvial incision and active surface uplift in the Woodlark Rift of eastern Papua New Guinea. *Lithosphere*, *4*(2), 131-149. https://doi.org/10.1130/L135.1

Miller, S. R., Sak, P. B., Kirby, E., & Bierman, P. R. (2013). Neogene rejuvenation of central Appalachian topography: Evidence for differential rock uplift from stream profiles and erosion rates. *Earth and Planetary Science Letters*, *369*, 1-12. https://doi.org/10.1016/j.epsl.2013.04.007

Miller, M. S., & Becker, T. W. (2014). Reactivated lithospheric-scale discontinuities localize dynamic uplift of the Moroccan Atlas Mountains. *Geology*, *42*(1), 35-38. https://doi.org/10.1130/G34959.1.

Miller, M. S., O'Driscoll, L. J., Butcher, A. J., & Thomas, C. (2015). Imaging Canary Island hotspot material beneath the lithosphere of Morocco and southern Spain. *Earth and Planetary Science Letters*, *431*, 186-194. https://doi.org/10.1016/j.epsl.2015.09.026

Missenard, Y., Zeyen, H., Frizon de Lamotte, D., Leturmy, P., Petit, C., Sébrier, M., & Saddiqi, O. (2006). Crustal versus asthenospheric origin of relief of the Atlas Mountains of Morocco. *Journal of Geophysical Research: Solid Earth*, *111*(B3). https://doi.org/10.1029/2005JB003708

Missenard, Y., Saddiqi, O., Barbarand, J., Leturmy, P., Ruiz, G., El Haimer, F. Z., & Frizon de Lamotte, D. (2008). Cenozoic denudation in the Marrakech High Atlas, Morocco: insight from apatite fission-track thermochronology. *Terra Nova*, *20*(3), 221-228. https://doi.org/10.1111/j.1365-3121.2008.00810.x.

Missenard, Y., & Cadoux, A. (2012). Can Moroccan Atlas lithospheric thinning and volcanism be induced by Edge-Driven Convection?. *Terra Nova*, *24*(1), 27-33. https://doi.org/10.1111/j.1365-3121.2011.01033.x

Molnar, P., & England, P. (1990). Late Cenozoic uplift of mountain ranges and global climate change: chicken or egg?. *Nature*, *346*(6279), 29-34. https://doi.org/10.1038/346029a0

Molnar, P. (2004). Late Cenozoic increase in accumulation rates of terrestrial sediment: How might climate change have affected erosion rates?. *Annu. Rev. Earth Planet. Sci.*, *32*, 67-89. https://doi.org/10.1146/annurev.earth.32.091003.143456

Montgomery, D. R., & Foufoula-Georgiou, E. (1993). Channel network source representation using digital elevation models. *Water Resources Research*, *29*(12), 3925-3934. https://doi.org/10.1029/93WR02463

Mudd, S. M., Attal, M., Milodowski, D. T., Grieve, S. W., & Valters, D. A. (2014). A statistical framework to quantify spatial variation in channel gradients using the integral method of channel profile analysis. *Journal of Geophysical Research: Earth Surface*, 119(2), 138-152. https://doi.org/10.1002/2013JF002981

Norton, K. P., von Blanckenburg, F., Schlunegger, F., Schwab, M., & Kubik, P. W. (2008). Cosmogenic nuclide-based investigation of spatial erosion and hillslope channel coupling in the transient foreland of the Swiss Alps. *Geomorphology*, 95(3-4), 474-486. https://doi.org/10.1016/j.geomorph.2007.07.013

Olivetti, V., Cyr, A. J., Molin, P., Faccenna, C., & Granger, D. E. (2012). Uplift history of the Sila Massif, southern Italy, deciphered from cosmogenic 10Be erosion rates and river longitudinal profile analysis. *Tectonics*, *31*(3). https://doi.org/10.1029/2011TC003037

Olivetti, V., Godard, V., Bellier, O., & ASTER team. (2016). Cenozoic rejuvenation events of Massif Central topography (France): Insights from cosmogenic denudation rates and river profiles. *Earth and Planetary Science Letters*, *444*, 179-191. https://doi.org/10.1016/j.epsl.2016.03.049

Palomeras, I., Thurner, S., Levander, A., Liu, K., Villaseñor, A., Carbonell, R., & Harnafi, M. (2014). Finite-frequency Rayleigh wave tomography of the western Mediterranean: Mapping its lithospheric structure. *Geochemistry, Geophysics, Geosystems*, *15*(1), 140-160. https://doi.org/10.1002/2013GC004861

Pastor, A., Babault, J., Owen, L. A., Teixell, A., & Arboleya, M. L. (2015). Extracting dynamic topography from river profiles and cosmogenic nuclide geochronology in the Middle Atlas and the High Plateaus of Morocco. *Tectonophysics*, *663*, 95-109. https://doi.org/10.1016/j.tecto.2015.06.007

Perron, J. T., & Royden, L. (2013). An integral approach to bedrock river profile analysis. *Earth Surface Processes and Landforms*, *38*(6), 570-576. https://doi.org/10.1002/esp.3302.

Pique, A., & Michard, A. (1989). Moroccan Hercynides; a synopsis; the Paleozoic sedimentary and tectonic evolution at the northern margin of West Africa. *American Journal of science*, *289*(3), 286-330. https://doi.org/10.2475/ajs.289.3.286

Piqué, A., Bouabdelli, M., Soulaimani, A., Youbi, N., & Illiani, M. (1999). Les conglomérats du PIII (Protérozoïque terminal) de l'Anti-Atlas (Sud du Maroc):

Molasses tardi-Panafricaines, ou marq n rifting fini-Protérozoïque. *Comptes Rendus Académie Sciences Paris*, *328*, 409-414.

Racano, S., Schildgen, T. F., Cosentino, D., & Miller, S. R. (2021). Temporal and spatial variations in rock uplift from river-profile inversions at the Central Anatolian Plateau southern margin. *Journal of Geophysical Research: Earth Surface*, *126*(8), e2020JF006027. https://doi.org/10.1029/2020JF006027

Rimi, A. (1999). Mantle heat flow and geotherms for the main geologic domains in Morocco. *International Journal of Earth Sciences*, *88*(3), 458-466. https://doi.org/10.1007/s005310050278

Royden, L., & Taylor Perron, J. (2013). Solutions of the stream power equation and application to the evolution of river longitudinal profiles. *Journal of Geophysical Research: Earth Surface*, *118*(2), 497-518. https://doi.org/10.1002/jgrf.20031

Safran, E. B., Bierman, P. R., Aalto, R., Dunne, T., Whipple, K. X., & Caffee, M. (2005). Erosion rates driven by channel network incision in the Bolivian Andes. *Earth Surface Processes and Landforms: The Journal of the British Geomorphological Research Group*, *30*(8), 1007-1024. https://doi.org/10.1002/esp.1259.

Scharf, T. E., Codilean, A. T., De Wit, M., Jansen, J. D., & Kubik, P. W. (2013). Strong rocks sustain ancient postorogenic topography in southern Africa. *Geology*, *41*(3), 331-334. https://doi.org/10.1130/G33806.1.

Schildgen, T. F., Cosentino, D., Bookhagen, B., Niedermann, S., Yıldırım, C., Echtler, H., ... & Strecker, M. R. (2012). Multi-phased uplift of the southern margin of the Central Anatolian plateau, Turkey: A record of tectonic and upper mantle processes. *Earth and Planetary Science Letters*, *317*, 85-95. https://doi.org/10.1016/j.epsl.2011.12.003

Schwanghart, W., & Scherler, D. (2014). TopoToolbox 2–MATLAB-based software for topographic analysis and modeling in Earth surface sciences. *Earth Surface Dynamics*, *2*(1), 1-7. https://doi.org/10.5194/esurf-2-1-2014.

Schwanghart, W., & Scherler, D. (2020). Divide mobility controls knickpoint migration on the Roan Plateau (Colorado, USA). *Geology*, *48*(7), 698-702. https://doi.org/10.1130/G47054.1

Seber, D., Barazangi, M., Tadili, B. A., Ramdani, M., Ibenbrahim, A., & Ben Sari, D. (1996). Three-dimensional upper mantle structure beneath the intraplate Atlas and interplate Rif mountains of Morocco. *Journal of Geophysical Research: Solid Earth*, *101*(B2), 3125-3138. https://doi.org/10.1029/95JB03112

Sébrier, M., Siame, L., Zouine, E. M., Winter, T., Missenard, Y., & Leturmy, P. (2006). Active tectonics in the moroccan high atlas. *Comptes Rendus Geoscience*, *338*(1-2), 65-79. https://doi.org/10.1016/j.crte.2005.12.001.

Sebti, S., Saddiqi, O., El Haimer, F. Z., Michard, A., Ruiz, G., Bousquet, R., Baidder, L., & de Lamotte, D. F. (2009). Vertical movements at the fringe of the West African Craton: First zircon fission track datings from the Anti-Atlas Precambrian basement, Morocco. *Comptes Rendus Geoscience*, *341*(1), 71-77. https://doi.org/10.1016/j.crte.2008.11.006

Sehrt, M., Glasmacher, U. A., Stockli, D. F., Jabour, H., & Kluth, O. (2018). The southern Moroccan passive continental margin: An example of differentiated long-term landscape evolution in Gondwana. *Gondwana Research*, *53*, 129-144. https://doi.org/10.1016/j.gr.2017.03.013

Sembroni, A., Molin, P., Pazzaglia, F. J., Faccenna, C., & Abebe, B. (2016). Evolution of continental-scale drainage in response to mantle dynamics and surface processes: An example from the Ethiopian Highlands. *Geomorphology*, 261, 12-29. https://doi.org/10.1016/j.geomorph.2016.02.022

Siame, L. L., Sébrier, M., Bellier, O., Bourlès, D., Costa, C., Ahumada, E. A., ... & Cisneros, H. (2015). Active basement uplift of Sierra Pie de Palo (Northwestern Argentina): rates and inception from10Be cosmogenic nuclide concentrations. *Tectonics*, *34*(6), 1129-1153. https://doi.org/10.1002/2014TC003771

Singer, B. S., Le Mével, H., Licciardi, J. M., Córdova, L., Tikoff, B., Garibaldi, N., ... & Feigl, K. L. (2018). Geomorphic expression of rapid Holocene silicic magma reservoir growth beneath Laguna del Maule, Chile. *Science advances*, *4*(6), eaat1513. https://doi.org/10.1126/sciadv.aat1513

Smith, A. G., Fox, M., Schwanghart, W., & Carter, A. (2022). Comparing methods for calculating channel steepness index. *Earth-Science Reviews*, 103970. https://doi.org/10.1016/j.earscirev.2022.103970

Snyder, N. P., Whipple, K. X., Tucker, G. E., & Merritts, D. J. (2000). Landscape response to tectonic forcing: Digital elevation model analysis of stream profiles in the Mendocino triple junction region, northern California. *Geological Society of America Bulletin*, *112*(8), 1250-1263. https://doi.org/10.1130/0016-7606(2000)112%3c1250:LRTTFD%3e2.0.CO;2

Soulaimani, A., Bouabdelli, M., & Piqué, A. (2003). L'extension continentale au Néo-Protérozoïque supérieur-Cambrien inférieur dans l'Anti-Atlas (Maroc). *Bulletin de la Société géologique de France*.

Soulaimani, A., & Burkhard, M. (2008). The Anti-Atlas chain (Morocco): the southern margin of the Variscan belt along the edge of the West African Craton. *Geological Society, London, Special Publications*, *297*(1), 433-452. https://doi.org/10.1144/SP297.20

Soulaimani, A., Michard, A., Ouanaimi, H., Baidder, L., Raddi, Y., Saddiqi, O., & Rjimati, E. C. (2014). Late Ediacaran–Cambrian structures and their reactivation during the Variscan and Alpine cycles in the Anti-Atlas (Morocco). *Journal of African Earth Sciences*, *98*, 94-112. https://doi.org/10.1016/j.jafrearsci.2014.04.025.

Spieker, K., Wölbern, I., Thomas, C., Harnafi, M., & El Moudnib, L. (2014). Crustal and upper-mantle structure beneath the western Atlas Mountains in SW Morocco derived from receiver functions. *Geophysical Journal International*, *198*(3), 1474-1485. https://doi.org/10.1093/gji/ggu216

Stäblein, G. (1988). Geomorphological aspects of the Quaternary evolution of the Ouarzazate Basin, southern Morocco. In *The Atlas System of Morocco* (pp. 433-444). Springer, Berlin, Heidelberg. DOI: https://doi.org/10.1007/BFb0011603

Stock, J. D., & Montgomery, D. R. (1999). Geologic constraints on bedrock river incision using the stream power law. *Journal of Geophysical Research: Solid Earth*, *104*(B3), 4983-4993. https://doi.org/10.1029/98JB02139.

Stock, J., & Dietrich, W. E. (2003). Valley incision by debris flows: Evidence of a topographic signature. *Water Resources Research*, *39*(4). https://doi.org/10.1029/2001WR001057

Teixell, A., Arboleya, M. L., Julivert, M., & Charroud, M. (2003). Tectonic shortening and topography in the central High Atlas (Morocco). *Tectonics*, *22*(5). https://doi.org/10.1029/2002TC001460

Teson, E., & Teixell, A. (2006). Sequence of thrusting and syntectonic sedimentation in the eastern Sub-Atlas thrust belt (Dades and Mgoun valleys, Morocco). *International Journal of Earth Sciences*, *97*(1), 103-113. https://doi.org/10.1007/s00531-006-0151-1

Tesón, E., Pueyo, E. L., Teixell, A., Barnolas, A., Agustí, J., & Furió, M. (2010). Magnetostratigraphy of the Ouarzazate Basin: Implications for the timing of deformation and mountain building in the High Atlas Mountains of Morocco. *Geodinamica Acta*, *23*(4), 151-165. https://doi.org/10.3166/ga.23.151-165

Thomas, R. J., Chevallier, L. P., Gresse, P. G., Harmer, R. E., Eglington, B. M., Armstrong, R. A., de Beer, C.H., Martini, J. E. J., Kock, G. S., Macey, P. H:, & Ingram, B. A. (2002). Precambrian evolution of the Sirwa window, Anti-Atlas orogen, Morocco. *Precambrian Research*, *118*(1-2), 1-57. https://doi.org/10.1016/S0301-9268(02)00075-X

Torsvik, T. H., Rousse, S., Labails, C., & Smethurst, M. A. (2009). A new scheme for the opening of the South Atlantic Ocean and the dissection of an Aptian salt basin. *Geophysical Journal International*, *177*(3), 1315-1333. https://doi.org/10.1111/j.1365-246X.2009.04137.x

Townsend, M. (2022). Linking surface deformation to thermal and mechanical magma chamber processes. *Earth and Planetary Science Letters*, *577*, 117272. https://doi.org/10.1016/j.epsl.2021.117272

Tucker, G. E., & van Der Beek, P. (2013). A model for post-orogenic development of a mountain range and its foreland. *Basin Research*, *25*(3), 241-259. https://doi.org/10.1111/j.1365-2117.2012.00559.x

Walsh, G. J., Aleinikoff, J. N., Benziane, F., Yazidi, A., & Armstrong, T. R. (2002). U–Pb zircon geochronology of the Paleoproterozoic Tagragra de Tata inlier and its Neoproterozoic cover, western Anti-Atlas, Morocco. *Precambrian Research*, *117*(1-2), 1-20. https://doi.org/10.1016/S0301-9268(02)00044-X

West, A. J., Fox, M., Walker, R. T., Carter, A., Harris, T., Watts, A. B., & Gantulga, B. (2013). Links between climate, erosion, uplift, and topography during intracontinental mountain building of the Hangay Dome, Mongolia. *Geochemistry, Geophysics, Geosystems*, *14*(12), 5171-5193. https://doi.org/10.1002/2013GC004859

Whipple, K. X., & Tucker, G. E. (1999). Dynamics of the stream-power river incision model: Implications for height limits of mountain ranges, landscape response timescales, and research needs. *Journal of Geophysical Research: Solid Earth*, *104*(B8), 17661-17674. https://doi.org/10.1029/1999JB900120.

Whipple, K. X., DiBiase, R. A., Ouimet, W. B., & Forte, A. M. (2017). Preservation or piracy: Diagnosing low-relief, high-elevation surface formation mechanisms. *Geology*, *45*(1), 91-94. https://doi.org/10.1130/G38490.1

Whittaker, A. C. (2012). How do landscapes record tectonics and climate?. *Lithosphere*, *4*(2), 160-164. https://doi.org/10.1130/RF.L003.1

Willett, S. D., & Brandon, M. T. (2002). On steady states in mountain belts. *Geology*, *30*(2), 175-178. https://doi.org/10.1130/0091-7613(2002)030%3c0175:OSSIMB%3e2.0.CO;2

Wilson, M., & Downes, H. (1991). Tertiary—Quaternary extension-related alkaline magmatism in western and central Europe. Journal of Petrology, 32(4), 811-849. https://doi.org/10.1093/petrology/32.4.811

Wobus, C., Whipple, K. X., Kirby, E., Snyder, N., Johnson, J., Spyropolou, K., Crosby, B., & Sheehan, D. (2006). Tectonics from topography: Procedures, promise, and pitfalls. *Special papers-Geological Society of America*, *398*, 55. https://doi.org/10.1130/2006.2398(04)

Wobus, C. W., Tucker, G. E., & Anderson, R. S. (2010). Does climate change create distinctive patterns of landscape incision?. *Journal of Geophysical Research: Earth Surface*, *115*(F4). https://doi.org/10.1029/2009JF001562

Yang, R., Willett, S. D., & Goren, L. (2015). In situ low-relief landscape formation as a result of river network disruption. *Nature*, *520*(7548), 526-529. https://doi.org/10.1038/nature14354

Zeyen, H., Ayarza, P., Fernàndez, M., & Rimi, A. (2005). Lithospheric structure under the western African-European plate boundary: A transect across the Atlas Mountains and the Gulf of Cadiz. *Tectonics*, 24(2). https://doi.org/10.1029/2004TC001639